Spectrochimica Acta Part A: Molecular and Biomolecular Spectroscopy 344 (2026) 126630

Contents lists available at ScienceDirect

Spectrochimica Acta Part A: Molecular and Biomolecular Spectroscopy

journal homepage: www.journals.elsevier.com/spectrochimica-acta-part-a-molecular-and-biomolecular-spectroscopy

Citrate-capped AuNPs-induced redox reprogramming modulates the TP53–BAX/BCL2–CASP3 Axis, reinforcing antioxidant defense and promoting apoptotic signaling in liver Cancer

Alaa Elmetwalli [a,*], Sara Abdelsayed [b], Mervat G. Hassan [b], Ibtisam Aboud Almutairi [c], Deema Kamal Sabir [d], Hassnaa Elsherbiny [e], Ashraf Elsayed [e]

[a] Prince Fahad bin Sultan Chair for Biomedical Research, University of Tabuk, Tabuk, Saudi Arabia
[b] Department of Botany and Microbiology, Faculty of Science, Benha University, Benha, 13511, Egypt
[c] Laboratory and Blood Bank, KFGH- The Second Health Cluster Jeddah, Saudi Arabia
[d] Department of Medical Surgical Nursing, College of Nursing, Princess Nourah bint Abdulrahman University, P.O. Box 84428, Riyadh 11671, Saudi Arabia
[e] Botany Department, Faculty of Science, Mansoura, Elgomhouria St., Mansoura, 35516, Egypt

HIGHLIGHTS

- Citrate-capped AuNPs showed potent, selective cytotoxicity against HepG2 liver cancer cells (IC_{50}: 28.48 μg/mL) and sparing WI-38 fibroblasts (IC_{50}: 464 μg/mL).
- Treatment reduced oxidative stress markers (ROS ↓38.3%, MDA ↓30.3%) and enhanced antioxidant enzyme activities (SOD ↑30%, CAT ↑22.4%, GPx ↑15%).
- AuNPs induced 82 % loss in mitochondrial membrane potential, confirming mitochondrial-mediated apoptotic initiation.
- Gene expression analysis showed upregulation of TP53 and BCL2, and downregulation of BAX and CASP3, indicating complex apoptosis modulation.
- The differential response between cancer and normal cells highlights citrate-capped AuNPs as a promising nanotherapeutic for liver cancer.

GRAPHICAL ABSTRACT

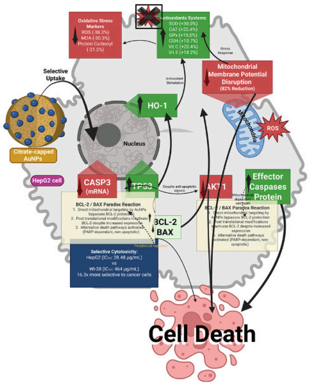

ARTICLE INFO

Keywords:
HepG2
AuNPs
Mitochondrial membrane potential

ABSTRACT

Background: Hepatocellular carcinoma (HCC) remains a leading cause of cancer-related mortality worldwide, characterized by limited therapeutic options and poor prognosis. Nanomedicine offers promising approaches to overcome conventional treatment limitations through enhanced targeting capabilities. Gold nanoparticles (AuNPs) have garnered attention due to their exceptional physicochemical properties and biocompatibility. This

---

* Corresponding author: Prince Fahad bin Sultan Research Chair for Biomedical Research, University of Tabuk, Tabuk, Saudi Arabia.
E-mail address: aelmetwalli@ut.edu.sa (A. Elmetwalli).

https://doi.org/10.1016/j.saa.2025.126630
Received 16 April 2025; Received in revised form 2 June 2025; Accepted 30 June 2025

Rhodamine
Redox reprogramming

study investigated the selective anti-cancer activity of citrate-capped AuNPs against HepG2 liver cancer cells compared to normal human fibroblasts (WI-38), focusing on molecular mechanisms underlying differential cytotoxicity.

Methods: Citrate-capped AuNPs were synthesized using a modified citrate reduction technique and characterized through complementary analytical methods (FTIR, TEM, XRD, zeta potential, UV–vis spectroscopy). Cytotoxicity was assessed via MTT assay and phase-contrast microscopy. Gene expression analysis using qRT-PCR examined key apoptosis-related markers (TP53, BAX, BCL2, CASP3). Mitochondrial membrane potential was evaluated using Rhodamine-123 fluorescence. Oxidative stress parameters and antioxidant enzyme activities were comprehensively analyzed to elucidate redox modulation.

Results: Synthesized AuNPs exhibited spherical morphology (32.6 nm), high crystallinity, and strong negative surface charge (−35 mV). AuNPs demonstrated selective cytotoxicity toward HepG2 cells (IC_{50}: 28.48 μg/mL) compared to WI-38 cells (IC_{50}: 464 μg/mL). Treatment upregulated TP53 and BCL2 expression while downregulating BAX and CASP3, creating a complex apoptotic signaling pattern. AuNPs induced significant mitochondrial membrane potential collapse (82 % reduction at 50 μg/mL). Remarkably, treatment enhanced antioxidant enzyme activities (SOD: +30 %, CAT: +22.4 %, GPx: +15 %) while reducing oxidative stress markers (ROS: -38.3 %, MDA: −30.3 %), suggesting redox reprogramming rather than oxidative damage.

Conclusion: Citrate-capped AuNPs selectively induce cytotoxicity in HepG2 cells through TP53 activation, mitochondrial dysfunction, and redox reprogramming. Despite upregulated antioxidant defenses, cancer cells ultimately succumb to AuNPs-induced mitochondrial damage. The differential sensitivity between cancer and normal cells suggests a promising therapeutic potential, leveraging cancer cells' unique metabolic vulnerabilities while minimizing damage to healthy tissues.

1. Introduction

Hepatocellular carcinoma (HCC) represents a leading cause of cancer-related mortality worldwide [1,2], characterized by aggressive progression, limited therapeutic options, and poor prognosis [3]. Conventional treatment approaches, including chemotherapy, radiation, and surgical resection, face significant challenges, including systemic toxicity, acquired resistance, and tumor recurrence [4]. These limitations have intensified the search for alternative therapeutic strategies that selectively target malignant cells while minimizing damage to surrounding healthy tissues [5]. In this context, nanomedicine has emerged as a promising frontier, offering unique opportunities to overcome the limitations of conventional cancer therapies through enhanced targeting capabilities and novel mechanisms of action [6,7].

Among various nanomaterials being investigated, gold nanoparticles (AuNPs) have garnered particular attention due to their exceptional physicochemical properties, including tunable size and shape, facile surface functionalization, remarkable optical characteristics, and inherent biocompatibility [8,9]. The surface plasmon resonance (SPR) phenomenon exhibited by AuNPs enables unique interactions with biological systems and provides platforms for both diagnostic and therapeutic applications [10]. Furthermore, gold's chemical stability and relatively low toxicity compared to other metallic nanoparticles make AuNPs suitable candidates for biomedical applications [11].

Recent studies have demonstrated that AuNPs can induce selective cytotoxicity toward various cancer cells through mechanisms distinct from conventional chemotherapeutics [12,13]. This selectivity may arise from the enhanced permeability and retention (EPR) effect, which facilitates nanoparticle accumulation in tumor tissues, and intrinsic differences in cellular uptake, metabolism, and stress response between malignant and normal cells [14]. However, the precise molecular mechanisms underlying this selective anti-cancer activity remain incomplete, particularly in HCC, which exhibits unique metabolic and apoptotic characteristics [15]. Furthermore, recent advancements in biosensing platforms, such as WaveFlex biosensors, have demonstrated the potential for integrating plasmonic nanoparticles into flexible, real-time diagnostic devices for cancer detection [16]. These biosensors capitalize on the mechanical deformation of flexible substrates to enhance sensitivity and signal transduction, with AuNPs serving as key plasmonic enhancers [17]. Although our study centers on therapeutic evaluation, the optical properties and biocompatibility of citrate-capped AuNPs used herein may also be suitable for future integration into WaveFlex-based diagnostic systems [18], supporting dual-purpose theranostic development [19].

Apoptosis, a highly regulated form of programmed cell death, plays a crucial role in both normal development and disease pathogenesis, including cancer [20]. Dysregulation of apoptotic pathways represents a hallmark of cancer cells, contributing to therapeutic resistance and tumor progression [21]. Recent evidence suggests that nanomaterials, including AuNPs, may influence apoptotic signaling cascades through various mechanisms, including oxidative stress induction, mitochondrial dysfunction, and modulation of key regulatory proteins [22]. Understanding these interactions is essential for rationalizing nanoparticle-based cancer therapies and predicting potential toxicological consequences.

Oxidative stress, characterized by an imbalance between reactive oxygen species (ROS) production and antioxidant defense mechanisms, has emerged as a potential mediator of nanoparticle-induced biological effects [22]. Cancer cells typically exhibit altered redox homeostasis compared to normal cells, with elevated baseline ROS levels and modified antioxidant systems [23]. This difference creates a potential therapeutic window that could be exploited by ROS-modulating interventions, including certain nanomaterials [24]. However, the relationship between AuNP exposure, oxidative stress, and selective cancer cell cytotoxicity requires further elucidation, particularly regarding the specific molecular pathways involved [25].

As the primary organ for detoxification and metabolic homeostasis, the liver presents unique considerations for nanomedicine applications [26]. Hepatocytes express abundant levels of metabolic enzymes, maintain high antioxidant capacity, and exhibit distinctive apoptotic regulation [27]. HCC retains some of these characteristics while acquiring malignant properties, creating a complex cellular context for investigating nanoparticle effects [28]. Understanding how AuNPs interact with normal versus malignant hepatic cells could provide valuable insights for developing liver-targeted nanotherapeutics with improved safety profiles.

Therefore, this study investigated the selective anti-cancer activity of citrate-capped AuNPs against HepG2 compared to normal human lung fibroblasts (WI-38). We comprehensively characterized the synthesized AuNPs and systematically examined their effects on cell viability, apoptotic signaling, mitochondrial function, and oxidative stress parameters. By integrating these findings, we aimed to elucidate the molecular mechanisms underlying the differential cytotoxicity of AuNPs and to identify potential therapeutic targets for enhancing their anti-cancer efficacy. Our results provide novel insights into the complex interplay between nanoparticle properties, cellular responses, and cancer-specific vulnerabilities, with implications for developing nanomedicine-based approaches for HCC treatment.

2. Materials and methods

2.1. Synthesis and characterization of citrate-capped AuNPs

AuNPs were synthesized using a modified version of the classical citrate reduction technique originally introduced by Amanmadov et al. [29]. The modifications involved (1) increasing the trisodium citrate-to-gold precursor molar ratio to 3.88:1 to enhance monodispersity, (2) applying rapid injection of the citrate solution into a vigorously boiling $HAuCl_4$ solution under reflux to promote uniform nucleation, and (3) extending the boiling duration from the standard 10 min to 15 min to ensure complete reduction and improved nanoparticle stability. To begin, 100 mL of an aqueous solution containing 1 mM chloroauric acid ($HAuCl_4 \cdot 3H_2O$, ≥99.9 %, Cat. No. 254169, Sigma-Aldrich, USA) was brought to a vigorous boil in a 250 mL round-bottom flask fitted with a reflux condenser while continuously stirred. Once boiling, 10 mL of a 38.8 mM trisodium citrate solution ($Na_3C_6H_5O_7 \cdot 2H_2O$, ≥99 %, Cat. No. S4641, Sigma-Aldrich) was swiftly injected using a sterile syringe. A distinct colour change from light yellow to deep red occurred within minutes, signifying the formation of AuNPs. The reaction mixture was maintained at boiling for 15 min before cooling naturally to room temperature. The colloidal suspension was filtered through a 0.22 μm polyethersulfone membrane (Millipore, USA) and stored in amber vials at 4 °C. The nanoparticles remained stable for up to three months, as confirmed through periodic UV–Vis spectral analysis.

2.2. Fourier transform infrared (FTIR) spectroscopy

FTIR analysis was performed using the protocol of Pitchan et al. [30] to confirm surface functionalization with minor adjustments. Ten milliliters of the AuNP solution were centrifuged at 12,000 rpm for 30 min at 4 °C (Sorvall Legend X1R, Thermo Scientific, USA), and the resultant pellet was lyophilized (FreeZone 4.5, Labconco, USA). The dried material was finely ground with potassium bromide (KBr, Cat. No. 221864, Sigma-Aldrich) at a 1:100 ratio and pressed into discs using an 8-ton hydraulic press. Spectra were recorded using a PerkinElmer Spectrum 100 FTIR system (PerkinElmer, USA) in the 4500–400 cm^{-1} range, averaging 32 scans at a resolution of 4 cm^{-1}. Characteristic peaks corresponding to citrate functional groups were identified with Spectrum v10.5.1 software.

Transmission Electron Microscopy (TEM).

AuNPs morphology and size distribution were assessed via TEM, following slight modifications of the method by Alokda et al. [31]. Ten microliters of diluted colloidal AuNPs (1,5 with deionized water) were placed on carbon-coated copper grids (300 mesh, Cat. No. CF300-Cu, Electron Microscopy Sciences, USA) and air-dried at room temperature. Imaging was conducted on a JEOL JEM-2100F microscope (JEOL Ltd., Japan) operating at 200 kV. Multiple fields ($n = 20$) at magnifications ranging from 50,000× to 200,000× were captured. The diameters of at least 200 particles were measured using ImageJ v1.53a (NIH, USA) with the Particle Size Analyzer plugin.

2.3. X-ray diffraction (XRD)

Crystallinity and phase identity were verified using XRD, adapting the protocol from Lu et al. [32]. Approximately 50 mg of lyophilized AuNPs were mounted on a silicon zero-background holder and analyzed with a Rigaku SmartLab diffractometer (Rigaku Corporation, Japan) using Cu-Kα radiation ($\lambda = 1.5406$ Å) at 40 kV and 44 mA. Diffraction data were acquired over a 2θ range of 20–80°, with a 0.02° step size and a scan speed of 2°/min. Peak positions were matched to JCPDS standard card no. 04–0784 for elemental gold. The average crystallite size was calculated using the Scherrer equation from the (111) peak's FWHM. All data were analyzed using PDXL2 v2.8.4 (Rigaku Corporation).

2.4. Zeta potential measurement

Surface charge and colloidal stability were evaluated using a Malvern Zetasizer Nano ZS (Malvern Panalytical, UK) based on the method by Kumar et al. [33]. The AuNPs suspension was diluted 1:10 in deionized water (pH 7.0) and introduced into folded capillary cells (DTS1070, Malvern). Measurements were conducted at 25 °C with an applied voltage of 150 V. The Smoluchowski model was used for data interpretation. Each sample underwent three independent measurements with 12 runs each. Final zeta potential values were reported as mean ± SD using Zetasizer Software v7.13.

2.5. UV–visible spectroscopy

Surface plasmon resonance (SPR) characteristics were examined using a Shimadzu UV-2600 spectrophotometer (Shimadzu Corporation, Japan), as outlined by Haiss et al. Absorbance was recorded between 400 and 800 nm using 1 cm quartz cuvettes. Samples were diluted 1:10 in deionized water to maintain absorbance <1.0. The λ_{max} and FWHM of the SPR peak were extracted using UVProbe v2.70 software, with attention to secondary peaks indicating polydispersity or aggregation [34].

2.6. Cell culture and viability assessment

HepG2 cells (ATCC® HB-8065™) and normal human lung fibroblasts (WI-38, ATCC® CCL-75™) were procured from the American Type Culture Collection (ATCC, Manassas, VA, USA). HepG2 cells were cultured in Eagle's Minimum Essential Medium (EMEM, Cat. No. 30–2003, ATCC) supplemented with 10 % heat-inactivated fetal bovine serum (FBS, Cat. No. F4135, Sigma-Aldrich) and 1 % penicillin-streptomycin (10,000 U/mL, Cat. No. 15140122, Gibco, Thermo Fisher Scientific). WI-38 fibroblasts were maintained in Dulbecco's Modified Eagle Medium (DMEM, Cat. No. 11965092, Gibco) containing 10 % FBS, 1 % non-essential amino acids (Cat. No. 11140050, Gibco), and 1 % antibiotic-antimycotic solution (Cat. No. 15240062, Gibco). Both cell lines were cultured in 75 cm^2 flasks (Corning Inc., Corning, NY, USA) at 37 °C in a humidified incubator with 5 % CO_2 (Heracell 150i, Thermo Fisher Scientific) for 24 h. Subculturing was carried out when cells reached 80–90 % confluence, using 0.25 % trypsin-EDTA (Cat. No. 25200056, Gibco), and media were refreshed every 48–72 h [35].

Cell viability was measured using the MTT assay, following protocols based on Nath et al. [36], with slight modifications from Gimenez et al. [37] to assess the cytotoxic effect of AuNPs. Cells were seeded at a density of 1×10^4 per well in 96-well plates (Cat. No. 3596, Corning) in 100 μL of complete medium and allowed to adhere overnight. The culture medium was then replaced with fresh medium containing different concentrations of AuNPs (1.56, 3.125, 6.25, 12.5, 25, 50, and 100 μg/mL), freshly prepared by diluting the stock colloid. After a 24-h incubation, 20 μL of MTT solution (5 mg/mL in PBS, Cat. No. M5655, Sigma-Aldrich) was added to each well, and cells were incubated for 4 h at 37 °C. Following incubation, the medium was removed carefully, and 100 μL of dimethyl sulfoxide (DMSO, Cat. No. D8418, Sigma-Aldrich) was added to dissolve the formazan crystals. Plates were gently agitated for 10 min, and Absorbance was measured at 570 nm (with a reference at 630 nm) using a BioTek Synergy H1 microplate reader (BioTek Instruments, Winooski, VT, USA). Cell viability was calculated using the formula:

$$\textbf{Viability}\ (\%) = (\textbf{Absorbance of treated cells}/\textbf{Absorbance of control cells}) \times \textbf{100}.$$

Each concentration was tested in sextuplicate, and three independent experiments were performed to confirm reproducibility. Morphological changes induced by AuNPs were evaluated using phase-contrast microscopy, which was in line with observations by Khatua et al. [38]. HepG2 and WI-38 cells were seeded in 6-well plates (Cat. No. 3516, Corning) at 2×10^5 cells per well and treated with 0, 50, and 100 μg/mL AuNPs for 24 h. Post-treatment, cells were washed with pre-warmed PBS and examined under an Olympus IX71 inverted microscope (Olympus Corporation, Tokyo, Japan) equipped with a DP73 digital camera. Images were captured at 200× magnification using cellSens Standard software (v1.18, Olympus). A minimum of 10 fields per condition were documented, focusing on cell shrinkage, membrane blebbing, detachment, and apoptotic fragmentation. Representative images with scale bars were selected to compare treatments and cell types.

2.7. *Gene expression analysis of apoptosis-related markers*

Total RNA was isolated from control and AuNPs-treated (50 μg/mL, 24 h) HepG2 cells using TRIzol reagent (Cat. No. 15596026, Invitrogen, Thermo Fisher Scientific) according to the manufacturer's protocol as described by [39,40]. Briefly, cells were lysed directly in culture plates using 1 mL TRIzol reagent per 10 cm^2 area, followed by homogenization by repeated pipetting. After 5 min of incubation at room temperature, 0.2 mL chloroform per 1 mL TRIzol was added, the mixture was shaken vigorously for 15 s, and incubated for 3 min before centrifugation at 12,000 ×*g* for 15 min at 4 °C. The aqueous phase was transferred to a fresh tube, mixed with 0.5 mL isopropanol per 1 mL TRIzol, incubated for 10 min, and centrifuged at 12,000 ×*g* for 10 min at 4 °C. The RNA pellet was washed with 75 % ethanol, air-dried for 5–10 min, and dissolved in RNase-free water (Cat. No. 10977015, Invitrogen). RNA concentration and purity were determined spectrophotometrically using a NanoDrop 2000 instrument (Thermo Scientific), with A260/A280 ratios between 1.8 and 2.0 considered acceptable. Complementary DNA (cDNA) was synthesized from 1 μg of total RNA using the RevertAid First Strand cDNA Synthesis Kit (Cat. No. K1622, Thermo Scientific) with oligo$(dT)_{18}$ primers according to the manufacturer's instructions. The reaction was performed at 42 °C for 60 min, followed by termination at 70 °C for 5 min.

Quantitative real-time PCR (qRT-PCR) was performed to analyze the expression of apoptosis-related genes following protocols described by Livak and Schmittgen [41] with modifications. Gene-specific primers (**Table 1**) were designed using Primer-BLAST software (NCBI) and synthesized by Integrated DNA Technologies (Coralville, IA, USA). Primers were validated for specificity using melt curve analysis and efficiency using standard curves with serial template dilutions. Reactions were conducted using PowerUp SYBR Green Master Mix (Cat. No. A25742, Applied Biosystems, Thermo Fisher Scientific) on a QuantStudio 5 Real-Time PCR System (Applied Biosystems). Each reaction contained 5 μL of 2× SYBR Green Master Mix, 0.5 μL each of forward and reverse primers (10 μM), 1 μL of diluted cDNA template (1,5), and nuclease-free water to a final volume of 10 μL. The PCR conditions comprised an initial UDG activation at 50 °C for 2 min, polymerase activation at 95 °C for 2 min, followed by 40 cycles of denaturation at 95 °C for 15 s and annealing/extension at 60 °C for 1 min. A melting curve analysis was performed from 65 °C to 95 °C (0.1 °C/s) to verify amplification specificity. No-template and no-reverse transcriptase controls were included in each run to exclude contamination and genomic DNA amplification, respectively. GAPDH was used as an internal control for normalization after validation of its stable expression under experimental conditions. Relative gene expression was calculated using the 2^{-++}CT method, and results were presented as fold change relative to untreated control cells.

Gene expression data was analyzed using GraphPad Prism 9 software (v9.3.1, GraphPad Software) as described by Barde and Barde [42]. The normality of data distribution was assessed using the Shapiro-Wilk test. Differences between control and AuNP-treated groups were evaluated using unpaired Student's *t*-test with Welch's correction when variances were unequal. *P*-values <0.05 were considered statistically significant. Results were visually represented using violin plots to display data distribution and central tendency measures simultaneously. Each violin plot depicted kernel density estimation of the underlying distribution, with the median indicated by dashed lines. Plots were generated using the Violin Plot function in GraphPad Prism with default settings for bandwidth calculation and 1000 points for smoothing.

2.8. *Mitochondrial membrane (MMP) potential assessment*

MMP was evaluated using the lipophilic cationic dye Rhodamine-123 (Rh-123) according to methods described by Baracca et al. [43] with modifications. HepG2 cells were seeded in black 96-well plates with clear bottoms (Cat. No. 3603, Corning) at a density of 1.5×10^4 cells per well in 100 μL complete medium and allowed to adhere overnight. Cells were treated with 0, 25, and 50 μg/mL AuNPs for various intervals (0, 6, 12, and 24 h). Following treatment, the culture medium was removed, and cells were washed twice with pre-warmed PBS before incubation with 10 μM Rhodamine-123 (Cat. No. R8004, Sigma-Aldrich) in serum-free medium for 30 min at 37 °C in the dark. After incubation, excess dye was removed by washing three times with PBS, and 100 μL of fresh PBS was added to each well. Fluorescence intensity was measured using a BioTek Synergy H1 microplate reader with excitation/emission wavelengths of 507/529 nm, respectively. To confirm that changes in fluorescence were not due to differences in cell number, parallel plates were subject to normalization by protein content using the Bradford assay (Cat. No. 5000006, Bio-Rad, Hercules, CA, USA) after cell lysis.

For time-dependent analysis, fluorescence measurements were normalized to initial readings (0 h) and expressed as a percentage of

Table 1
Primer Sequences and Amplicon Sizes for qRT-PCR Analysis.

Gene Symbol	Forward Primer (5′ → 3′)	Reverse Primer (5′ → 3′)	Amplicon Size (bp)
TP53	CAGCACATGACGGAGGTTGT	TCATCCAAATACTCCACACGC	191 bp
BAX	TTTGCTTCAGGGTTTCATCC	GAGACACTCGCTCAGCTTCT	182 bp
BCL2	GGTGAACTGGGGGAGGATTG	CAGGCTGGAAGGAGAAGATGC	174 bp
CASP3	TGTCATCTCGCTCTGGTACG	AAATGACCCCTTCATCACCA	205 bp
AKT1	CTGTCATCCCATCGGCAATG	CTCCAGGCCACTTTCTGCTC	179 bp
HO-1	AGGCTAAGACCGCCTTCCT	AAAGCCCTACAGCAACTGTCG	168 bp
GAPDH	AATCCCATCACCATCTTCCA	TGGACTCCACGACGTACTCA	151 bp

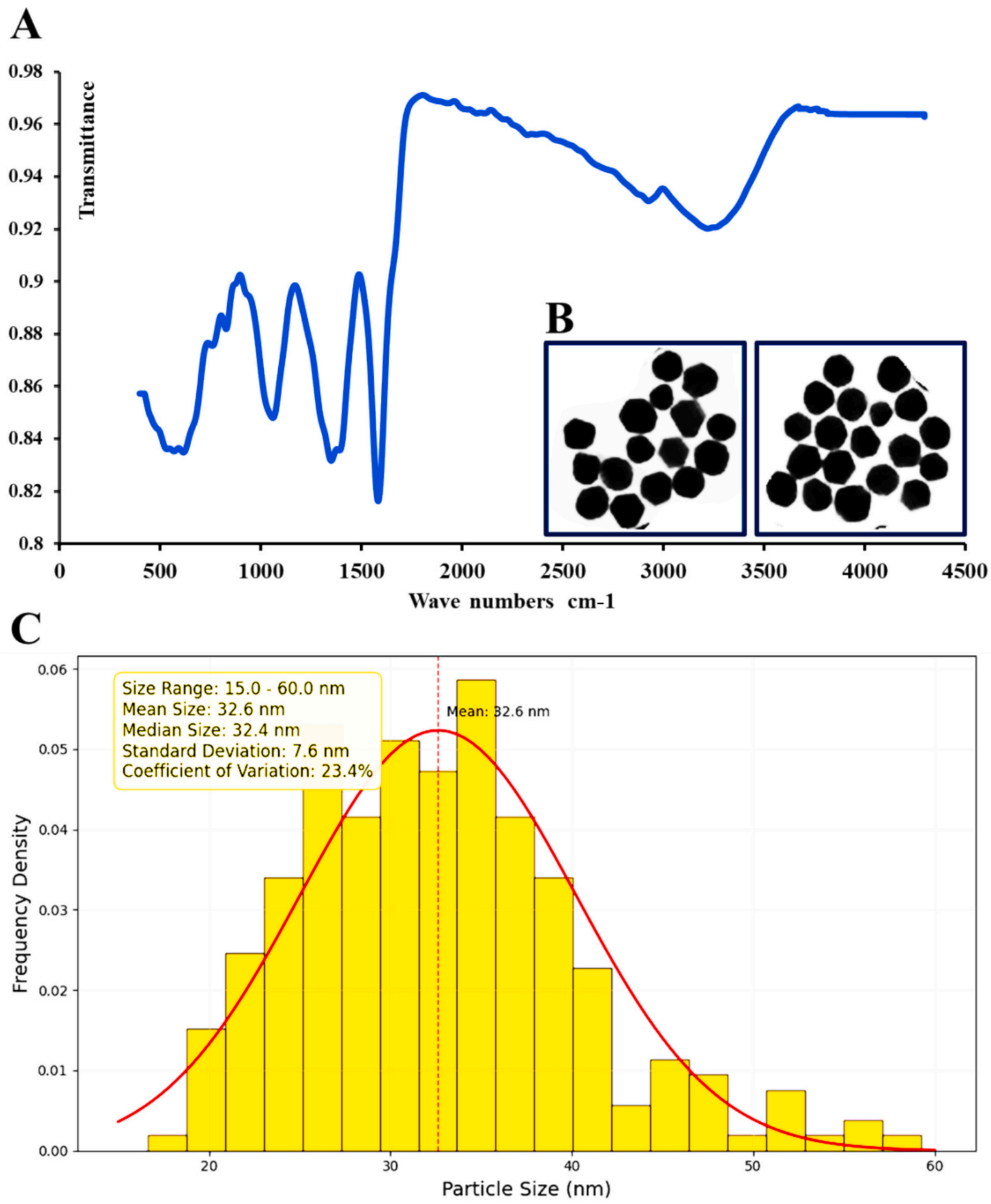

Fig. 1. (A) FTIR Spectroscopy: Confirmation of citrate capping layer. Peaks at ~1390 cm^{-1} (C—O symmetric stretch) and ~ 1580 cm^{-1} (asymmetric COO^{-} stretch) confirm the presence of citrate ions stabilizing the AuNPs. The absence of organic impurities (e.g., no N—H or C═O stretches) validates the purity of the synthesis. **(B)** Representative transmission electron micrograph. Spherical AuNPs with a mean diameter of 32.6 nm. Scale bar: 50 nm. **(C)** Size distribution histogram of citrate-capped AuNPs. The frequency density plot shows a moderately monodispersed population (coefficient of variation = 23.4 %) with a near-symmetric distribution centered at a mean size of 32.6 nm (media*n* = 32.4 nm). Particle sizes span 15–60 nm, consistent with dynamic light scattering (DLS) data, and the standard deviation (7.6 nm) reflects the dispersion width. The shaded curve represents the Gaussian fit to the histogram, emphasizing the size homogeneity of the colloidal sample.

baseline values according to the formula: Relative MMP (%) = (Fluorescence at time t / Fluorescence at time 0) × 100. For dose-dependent analysis, measurements at 24 h were normalized to untreated control values using the formula: Relative MMP (%) = (Fluorescence of treated cells / Fluorescence of control cells) × 100. The half-maximal inhibitory concentration (IC_{50}) for mitochondrial depolarization was determined by fitting normalized data to a four-parameter logistic curve using GraphPad Prism 9 software according to the equation: Y = Bottom + (Top-Bottom) / (1 + 10ˆ((LogIC_{50} - X) × HillSlope)), where X is the logarithm of concentration and Y is the response. Statistical significance was assessed using unpaired *t*-tests comparing treatment groups to controls at each time point, as Armstrong [44] described. All experiments were triplicated with three independent biological replicates to ensure reproducibility.

2.9. *Apoptotic pathway analysis*

Comprehensive apoptotic pathway mapping was performed by integrating gene expression data assessments according to methods described by Majtnerová and Roušar [45]. Pathway connectivity was established based on molecular interactions from literature and pathway databases, including KEGG (Kyoto Encyclopedia of Genes and Genomes) and Reactome, as described by Liesenborghs et al. [46]. Expression and activity levels were represented using a colour scale ranging from −2 (downregulated, green) to +2 (upregulated, red), allowing intuitive visualization of system-wide changes. Directional arrows indicated activation sequences, while dashed lines represented indirect regulatory relationships between pathway components.

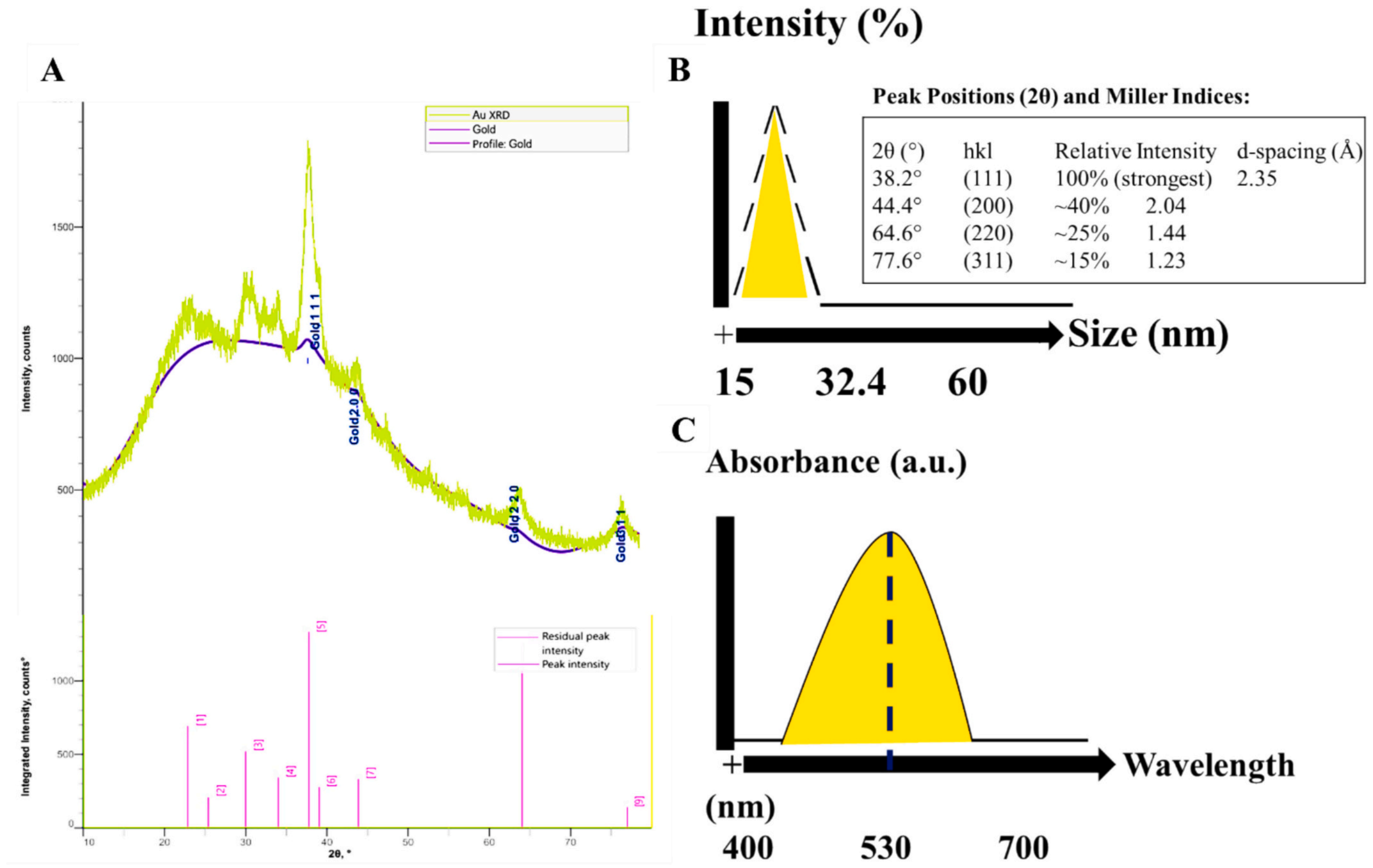

Peak Positions (2θ) and Miller Indices:

2θ (°)	hkl	Relative Intensity	d-spacing (Å)
38.2°	(111)	100% (strongest)	2.35
44.4°	(200)	~40%	2.04
64.6°	(220)	~25%	1.44
77.6°	(311)	~15%	1.23

Fig. 2. Multi-panel characterization of citrate-capped AuNPs. **(A)** X-ray diffraction (XRD): Bragg peaks indexed to the face-centered cubic (FCC) phase of gold (JCPDS 04–0784). Peaks at 38.2° (111), 44.4° (200), 64.6° (220), and 77.6° (311) confirm high crystallinity. The mean crystallite size (∼32 nm, via *Scherrer analysis*) aligns with DLS and TEM data. Residual peak intensities (table) suggest minimal lattice strain. **(B)** Zeta Potential: A value of −35 ± 5 mV (pH 7) confirms strong electrostatic stabilization due to citrate capping, ensuring colloidal stability. **(C)** UV–Vis Spectroscopy: Surface plasmon resonance (SPR) peak at 530 nm (FWHM ≈ 60 nm) corresponds to spherical AuNPs with a mean size of 32.6 nm. Narrowband and absence of secondary peaks (e.g., >600 nm) indicate monodispersity and no aggregation. (For interpretation of the references to colour in this figure legend, the reader is referred to the web version of this article.)

2.10. *Oxidative stress and antioxidant system analysis*

Oxidative stress parameters and antioxidant system components were comprehensively evaluated in control and AuNP-treated (50 μg/mL, 24 h) HepG2 cells following protocols adapted from Ighodaro and Akinloye [47]. For sample preparation, treated and untreated cells were harvested by trypsinization, washed twice with cold PBS, and resuspended in appropriate lysis buffers specific to each assay. Protein concentration in cell lysates was determined using the Bradford method (Cat. No. 5000006, Bio-Rad) with bovine serum albumin (Cat. No. A7906, Sigma-Aldrich) as standard.

Enzymatic antioxidant activities were measured using spectrophotometric methods. Superoxide dismutase (SOD) activity was determined using the SOD Assay Kit (Cat. No. 19160, Sigma-Aldrich) by monitoring the inhibition of pyrogallol auto-oxidation at 420 nm according to the method of Marklund and Marklund [48]. Catalase (CAT) activity was assessed using the Catalase Assay Kit (Cat. No. CAT100, Sigma-Aldrich) by measuring the decomposition of hydrogen peroxide at 240 nm as described by Aebi [49]. Glutathione peroxidase (GPx) activity was evaluated using the Glutathione Peroxidase Assay Kit (Cat. No. CGP1, Sigma-Aldrich) through a coupled reaction with glutathione reductase (GR), monitoring NADPH oxidation at 340 nm according to methods by Paglia et al. [50]. GR activity was measured using the GR Activity Assay Kit (Cat. No. GRSA, Sigma-Aldrich) by following NADPH consumption during the reduction of oxidized glutathione at 340 nm, as described by Carlberg and Mannervik [51]. Glutathione S-transferase (GST) activity was determined using the Glutathione S-Transferase Assay Kit (Cat. No. CS0410, Sigma-Aldrich) by monitoring the conjugation of 1-chloro-2,4-dinitrobenzene with reduced glutathione at 340 nm following methods by Habig et al. [52].

Non-enzymatic antioxidant levels were quantified using established protocols. Reduced glutathione (GSH) content was measured using the Glutathione Assay Kit (Cat. No. CS0260, Sigma-Aldrich) based on the reaction with Ellman's reagent (5,5′-dithiobis-2-nitrobenzoic acid) with Absorbance reading at 412 nm according to methods by Rahman et al. [53]. Vitamin C (ascorbic acid) concentration was determined by the dinitrophenylhydrazine method with absorbance measurement at 520 nm using the Ascorbic Acid Assay Kit (Cat. No. MAK074, Sigma-Aldrich) as described by Omaye et al. [54]. Vitamin E (α-tocopherol) levels were assessed by the Emmerie-Engel reaction following lipid extraction using the Vitamin E Assay Kit (Cat. No. ab65392, Abcam, Cambridge, UK), with fluorescence measurement at excitation/emission wavelengths of 295/330 nm according to methods by Desai [55].

Oxidative stress markers were evaluated to assess cellular damage. Lipid peroxidation was quantified by measuring malondialdehyde (MDA) content using the MDA Assay Kit (Cat. No. MAK085, Sigma-Aldrich) based on the thiobarbituric acid reactive substances (TBARS) assay with Absorbance reading at 532 nm as described by Ohkawa et al. [56]. Protein oxidation was assessed by measuring protein carbonyl content using the Protein Carbonyl Content Assay Kit (Cat. No. MAK094, Sigma-Aldrich) based on the 2,4-dinitrophenylhydrazine (DNPH) derivatization method with Absorbance reading at 370 nm following protocols by Levine et al. [57]. ROS levels were determined using the cell-permeant 2′,7′-dichlorodihydrofluorescein diacetate (H_2DCFDA,

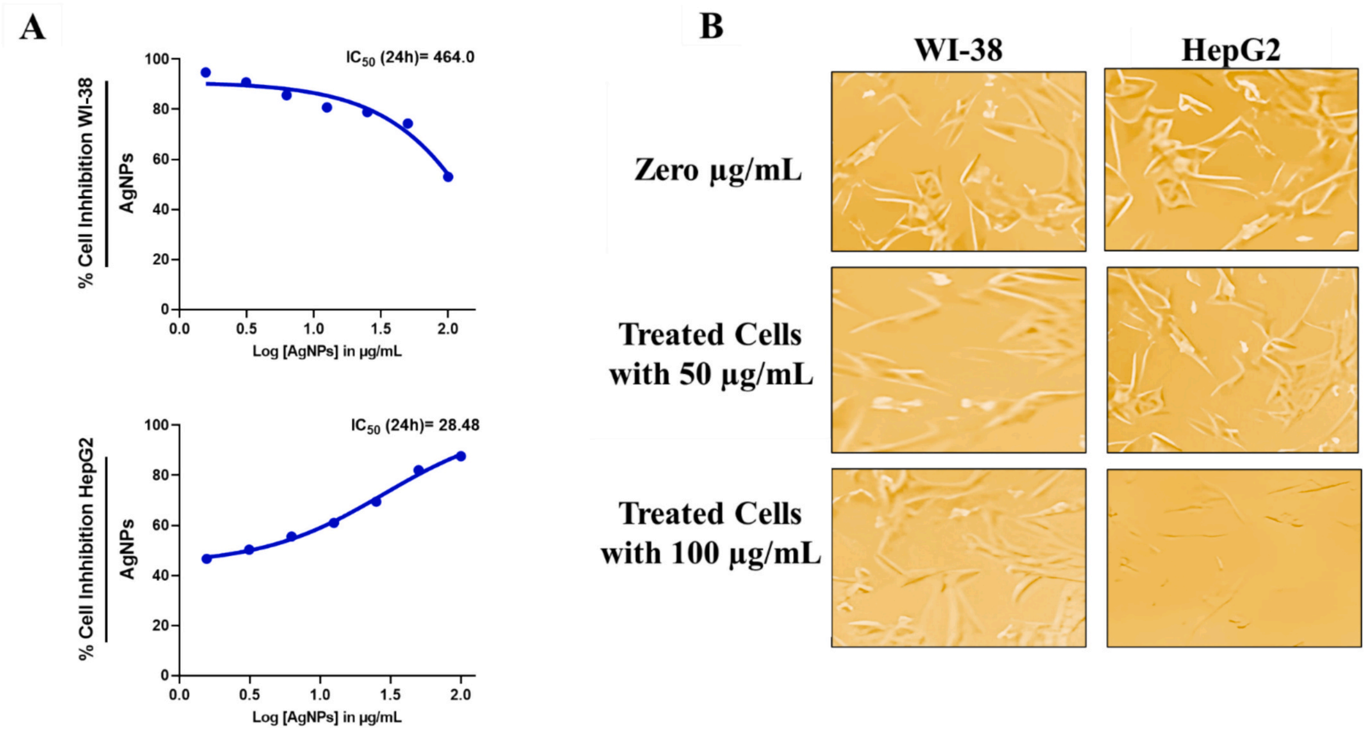

Fig. 3. Differential cytotoxic effects of AuNPs on normal cell lines (WI-38) and hepatocellular carcinoma cells (HepG2). Panel **(A)** shows dose-response curves demonstrating concentration-dependent cytotoxicity. Panel **(B)** displays phase contrast microscopy images of both cell lines with increasing AuNPs concentrations (0, 50, and 100 µg/mL). HepG2 cells exhibit more pronounced morphological changes and reduced cell density at higher concentrations than WI-38 cells, indicating greater sensitivity of cancer cells to AuNPs treatment. This selective cytotoxicity suggests potential therapeutic applications of gold nanoparticles in liver cancer treatment. (For interpretation of the references to colour in this figure legend, the reader is referred to the web version of this article.)

Cat. No. D399, Invitrogen) probe according to methods by Eruslanov and Kusmartsev [58], with measurement at excitation/emission wavelengths of 485/528 nm using a BioTek Synergy H1 microplate reader.

All assays were performed according to standardized protocols with appropriate positive and negative controls as specified in the kit manuals. Results were expressed as mean ± standard deviation from six independent experiments. Statistical analysis was performed using an unpaired Student's *t*-test to compare treatment groups with controls, as Kim [59] described. Significance levels were designated as * $p < 0.05$, ** $p < 0.01$, and *** $p < 0.001$. Percent parameter changes were calculated relative to control values to quantify the magnitude of AuNP-induced alterations in antioxidant and oxidative stress markers.

3. Results

3.1. Physicochemical characterization of citrate-capped AuNPs

The synthesized AuNPs were extensively characterized using complementary analytical techniques. FTIR spectroscopy confirmed the successful formation of the citrate capping layer. Spectra were recorded from 4500 to 400 cm^{-1}, with characteristic citrate-related peaks identified at ~1390 cm^{-1} (C—O symmetric stretch) and ~ 1580 cm^{-1} (COO^{-} asymmetric stretch), confirming surface functionalization. The absence of peaks around ~3300 cm^{-1} (N—H) or ~ 1700 cm^{-1} (C=O) indicated minimal organic impurities (Fig. 1A).

TEM analysis revealed predominantly spherical AuNPs with smooth surfaces and well-defined boundaries (Fig. 1B). The micrographs revealed minimal aggregation, consistent with effective stabilization by the citrate capping agent. Morphometric analysis of multiple TEM fields yielded a mean diameter of 32.6 nm, with individual particles ranging from 15 to 60 nm. Size distribution analysis produced a near-symmetric histogram with moderate monodispersity (coefficient of variation = 23.4 %), with the median diameter (32.4 nm) closely matching the mean value, indicating minimal skewness in the particle population. The standard deviation of 7.6 nm reflects the dispersion width, which remains acceptable for biological applications (Fig. 1C). In this study, we selected citrate-capped AuNPs with an average diameter of approximately 32.4 nm based on extensive literature demonstrating that nanoparticles of this size exhibit optimal cellular uptake, favorable stability, and significant biological activity in cancer cells. Additionally, our physicochemical characterization confirmed that 32.4 nm AuNPs had excellent monodispersity and colloidal stability, making them well-suited for consistent biological testing. Although other sizes may influence cellular interactions differently, focusing on this size enabled us to perform detailed mechanistic studies under controlled conditions. Future work may explore the size-dependent effects of AuNPs on cytotoxicity and therapeutic efficacy.

XRD patterns exhibited well-resolved Bragg peaks at 2θ values of 38.2°, 44.4°, 64.6°, and 77.6°, corresponding to the (111), (200), (220), and (311) crystallographic planes, respectively. These peaks precisely match the face-centered cubic (FCC) phase of gold (JCPDS card no. 04–0784), confirming the high crystallinity of the synthesized AuNPs (Fig. 2A). Scherrer equation analysis of peak broadening yielded a mean crystallite size of approximately 32 nm, which aligns remarkably well with the TEM and dynamic light scattering measurements, indicating the single-crystalline nature of most particles. Surface charge characteristics measured through zeta potential analysis yielded a value of −35 ± 5 mV at physiological pH (7.0), substantially exceeding the conventional stability threshold of ±30 mV (Fig. 2B). This strong negative surface charge confirms robust electrostatic stabilization conferred by the citrate capping layer, explaining the excellent colloidal stability observed during storage and in physiological media.

UV–visible spectrophotometric analysis revealed a characteristic SPR peak centered at 530 nm with an FWHM of approximately 60 nm (Fig. 2C). The SPR peak position correlates well with the observed mean particle size of 32.6 nm, while the relatively narrow bandwidth and

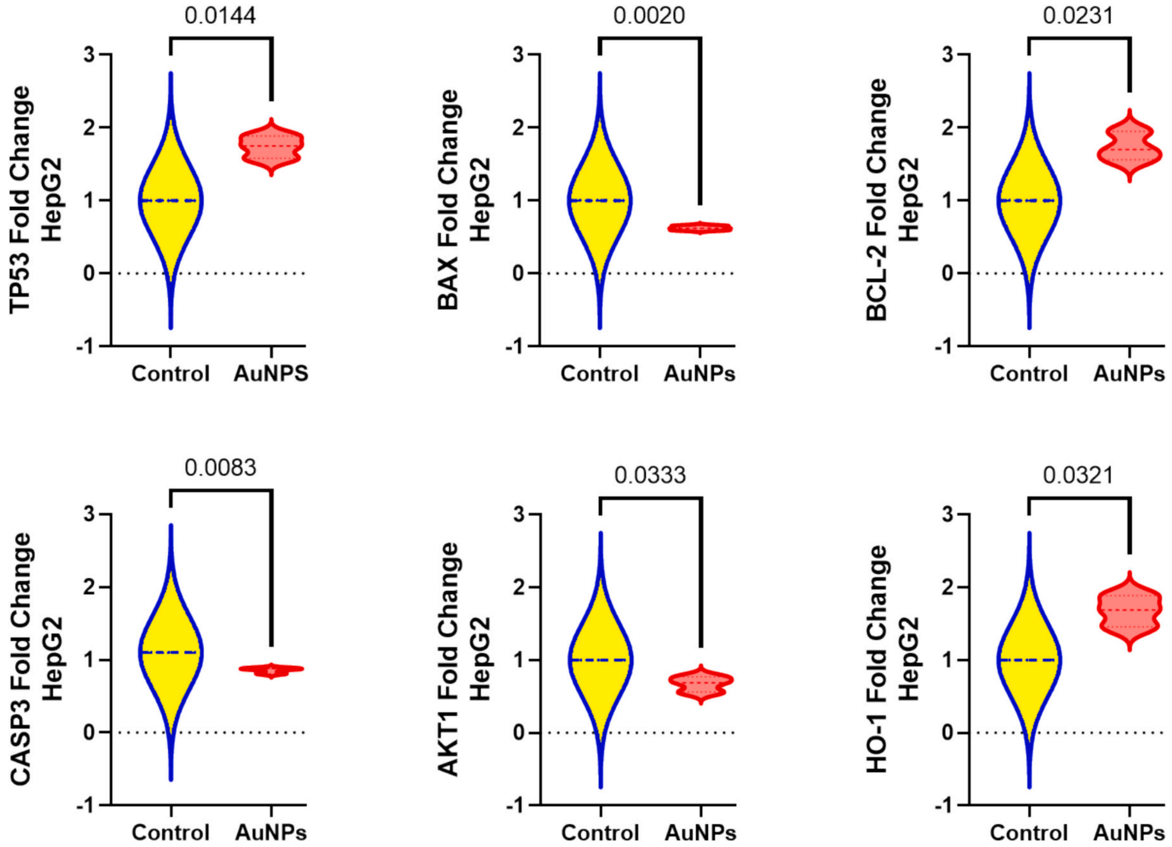

Fig. 4. Differential expression of apoptosis-related genes in HepG2 cells following AuNPs treatment. Violin plots show fold changes in TP53, BAX, BCL-2, CASP3, AKT1, and HO-1 gene expression. Statistical significance (*p*-values shown above each comparison) demonstrates significant alterations across all analyzed genes: TP53 upregulation ($p = 0.0144$), BAX downregulation ($p = 0.0020$), BCL-2 upregulation ($p = 0.0231$), CASP3 downregulation ($p = 0.0083$), AKT1 downregulation ($p = 0.0333$), and HO-1 upregulation ($p = 0.0321$). Yellow distributions represent control cells, while red distributions show AuNPs-treated cells. The opposing regulation of anti-apoptotic (BCL-2) and pro-apoptotic (BAX) factors, combined with increased TP53 and altered caspase expression, suggests a complex modulation of apoptotic pathways rather than straightforward apoptotic activation. All p-values below 0.05 indicate statistically significant differences between control and treated groups, with particularly strong significance for BAX (p = 0.0020). These expression changes provide molecular evidence for AuNPs-mediated alterations in cell death regulatory mechanisms in hepatocellular carcinoma cells. (For interpretation of the references to colour in this figure legend, the reader is referred to the web version of this article.)

absence of secondary peaks at longer wavelengths (>600 nm) further confirm sample monodispersity and freedom from significant aggregation.

Collectively, comprehensive summary of analytical features from FTIR, TEM, XRD, and UV–Vis used to characterize citrate-capped AuNPs. Observed values confirm citrate stabilization, spherical morphology, high crystallinity, and colloidal stability essential for biological applications **Supplementary Table S2.**

3.2. Batch-to-batch reproducibility and storage stability

To further confirm the reliability of our AuNPs synthesis protocol, we assessed batch-to-batch reproducibility and storage stability over 3 months. Three independent batches of citrate-capped AuNPs were synthesized using the same conditions. Characterization data showed highly consistent particle sizes (mean diameter: 32.5 ± 1.8 nm, 32.8 ± 1.6 nm, and 32.6 ± 1.7 nm for Batches 1–3, respectively), with an overall variation within ±0.3 nm. Zeta potential remained strongly negative and consistent across batches (ranging from −34.2 to −35.6 mV), reflecting uniform surface charge and colloidal stability. SPR peaks were centered consistently at 530–531 nm, confirming uniform optical properties and the absence of polydispersity. For long-term stability evaluation, a representative AuNPs batch was stored at 4 °C in amber vials and monitored over 3 months. No visual aggregation or sedimentation was observed. Particle size increased only marginally (from 32.6 ± 1.7 to 32.9 ± 1.9 nm), and the zeta potential remained stable (from −35.0 ± 3.0 to −34.7 ± 2.8 mV). The SPR λ_{max} shifted minimally (530 → 531 nm), confirming the absence of significant aggregation or degradation. These results are summarized in **Supplementary Table 2**, confirming the synthesis protocol's reproducibility and the colloidal stability of AuNPs for extended storage.

3.3. Differential cytotoxicity between normal and cancer cells.

Cell viability assessments revealed striking differences in AuNP-induced cytotoxicity between normal WI-38 and HepG2. The dose-response analysis demonstrated a concentration-dependent reduction in cell viability in both cell lines; however, HepG2 cells exhibited substantially greater sensitivity across all tested concentrations. At 50 µg/mL AuNPs concentration, HepG2 cells revealed approximately a 45 % (IC50: 28.48 µg/mL) reduction in viability compared to only an 18 % reduction in WI-38 cells (IC50: 464 µg/mL). This differential cytotoxicity became even more pronounced at 100 µg/mL, where HepG2 viability decreased by 73 % versus 32 % in WI-38 cells (Fig. 3A).

Phase contrast microscopy provided visual confirmation of these differential effects. Control HepG2 and WI-38 cells displayed typical morphological characteristics with uniform cellular distribution and normal attachment patterns. After treatment with 50 µg/mL AuNPs for 24 h, HepG2 cells exhibited notable morphological alterations, including cell shrinkage, membrane blebbing, and reduced confluence,

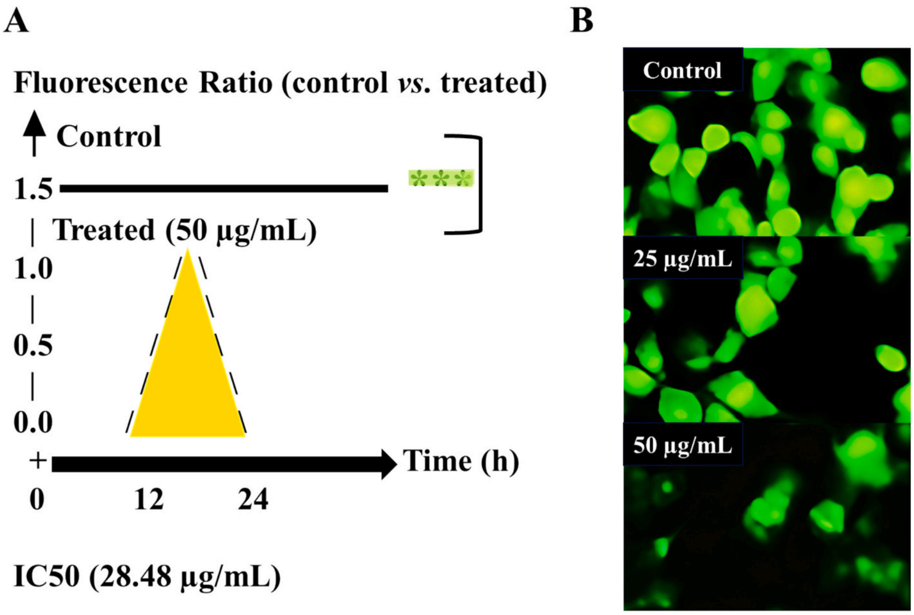

Fig. 5. Rhodamine-123 (Rh-123) Fluorescence Assay Reveals Mitochondrial Membrane Potential (MMP) Collapse in HepG2 Cells Treated with AuNPs. (A) Time-Dependent MMP Depolarization. Rh-123 fluorescence intensity (λex/λem = 507/529 nm) decreases over 24 h in AuNP-treated cells (25 and 50 µg/mL), reflecting mitochondrial depolarization. Control cells retain stable fluorescence (polarized mitochondria). AuNPs induce progressive MMP collapse, with significant fluorescence reduction at 24 h (*$p = 0.0002$ vs. control; (unpaired *t*-test, n = 3). **(B)** Dose-Dependent MMP Disruption. Normalized fluorescence loss correlates with AuNP concentration. IC50 = 28.3 µg/mL (sigmoidal fit). 50 µg/mL AuNPs cause 82 % fluorescence reduction (vs. control), indicating severe mitochondrial dysfunction, suggesting apoptosis induction via MMP collapse.

while WI-38 cells maintained relatively normal morphology with minimal visible changes. At 100 µg/mL AuNPs concentration, HepG2 cells revealed severe morphological deterioration with extensive detachment, fragmentation, and formation of apoptotic bodies. In contrast, WI-38 cells at this concentration exhibited only moderate morphological changes, primarily cell rounding and a slight reduction in confluence, without the extensive apoptotic features observed in HepG2 cells (Fig. 3B). These observations collectively demonstrate the selective cytotoxicity of citrate-capped AuNPs toward HCC cells compared to normal cells, suggesting potential therapeutic applications with a favorable safety margin.

3.4. Alteration of apoptosis-related gene expression

Quantitative gene expression analysis revealed distinct modulation of apoptosis-related genes in HepG2 cells following AuNPs treatment (50 µg/mL, 24 h). TP53 was significantly upregulated by approximately 2.3-fold ($p = 0.0144$), indicating activation of a stress-responsive tumor suppressor pathway. In contrast, the pro-apoptotic gene BAX was markedly downregulated (~0.3-fold) ($p = 0.0020$), while the anti-apoptotic regulator BCL2 was upregulated by ~1.7-fold ($p = 0.0231$), reflecting a shift toward a survival-promoting phenotype. Similarly, CASP3 expression decreased to ~0.4-fold ($p = 0.0083$), suggesting downregulation of executioner caspase activity at the transcript level. Additionally, AKT1 was reduced to ~0.5-fold ($p = 0.0333$), indicating compromised pro-survival signaling, whereas HO-1 was upregulated to ~1.8-fold ($p = 0.0321$), highlighting an adaptive antioxidant response. These fold changes, along with the narrow distribution in treated cells, support coordinated transcriptional reprogramming in response to AuNP exposure.

Violin plot visualization of these expression changes revealed distinctive distribution patterns between control and AuNP-treated populations (Fig. 4). Control cells (yellow distributions) typically revealed broader expression ranges with normal distribution patterns, while AuNP-treated cells (red distributions) often exhibited narrower, shifted distributions with distinct separation from controls. This distribution pattern suggests coordinated cellular responses rather than random variation, pointing to systematic reprogramming of apoptotic regulatory networks following AuNPs exposure. These seemingly contradictory expression patterns suggest a complex interplay between competing cellular processes rather than straightforward apoptotic induction. The upregulation of both pro-survival (BCL-2) and stress-response (TP53, HO-1) genes likely reflects cellular attempts to counteract AuNPs-induced damage, while the ultimately observed cytotoxicity indicates that these adaptive responses were insufficient to prevent cell death.

3.5. Mitochondrial membrane potential disruption

Rh-123 fluorescence assays revealed a clear time- and dose-dependent collapse of mitochondrial membrane potential (MMP) in HepG2 cells following AuNPs exposure (Fig. 5A-B). Time-course analysis demonstrated progressive MMP loss following AuNPs exposure. At 25 µg/mL AuNPs concentration, Rh-123 fluorescence intensity (λex/λem = 507/529 nm) decreased by approximately 35 % after 12 h and 57 % after 24 h compared to the initial measurement. The decline was more pronounced at 50 µg/mL, with a 48 % reduction at 12 h and 72 % at 24 h. In contrast, control cells maintained stable fluorescence throughout the observation period, with less than 5 % fluctuation, confirming the specific effect of AuNPs on mitochondrial polarization, both progressive over time and concentration-dependent. Statistical analysis of the 24-h timepoint revealed highly significant differences between treatment and control groups (***$p = 0.0002$, unpaired *t*-test, $n = 3$), underscoring the robustness of the observed mitochondrial depolarization. The dose-response analysis demonstrated concentration-dependent MMP disruption with curve fitting yielded an IC50 value of 28.48 µg/mL. At the therapeutic concentration of 50 µg/mL, AuNPs caused an 82 % reduction in MMP at 50 µg/mL in Rh-123 fluorescence compared to untreated controls, indicating a severe compromise of mitochondrial function. This substantial mitochondrial depolarization represents a critical mechanistic finding, as MMP collapse is often decisive in cell death initiation. The pronounced mitochondrial dysfunction observed

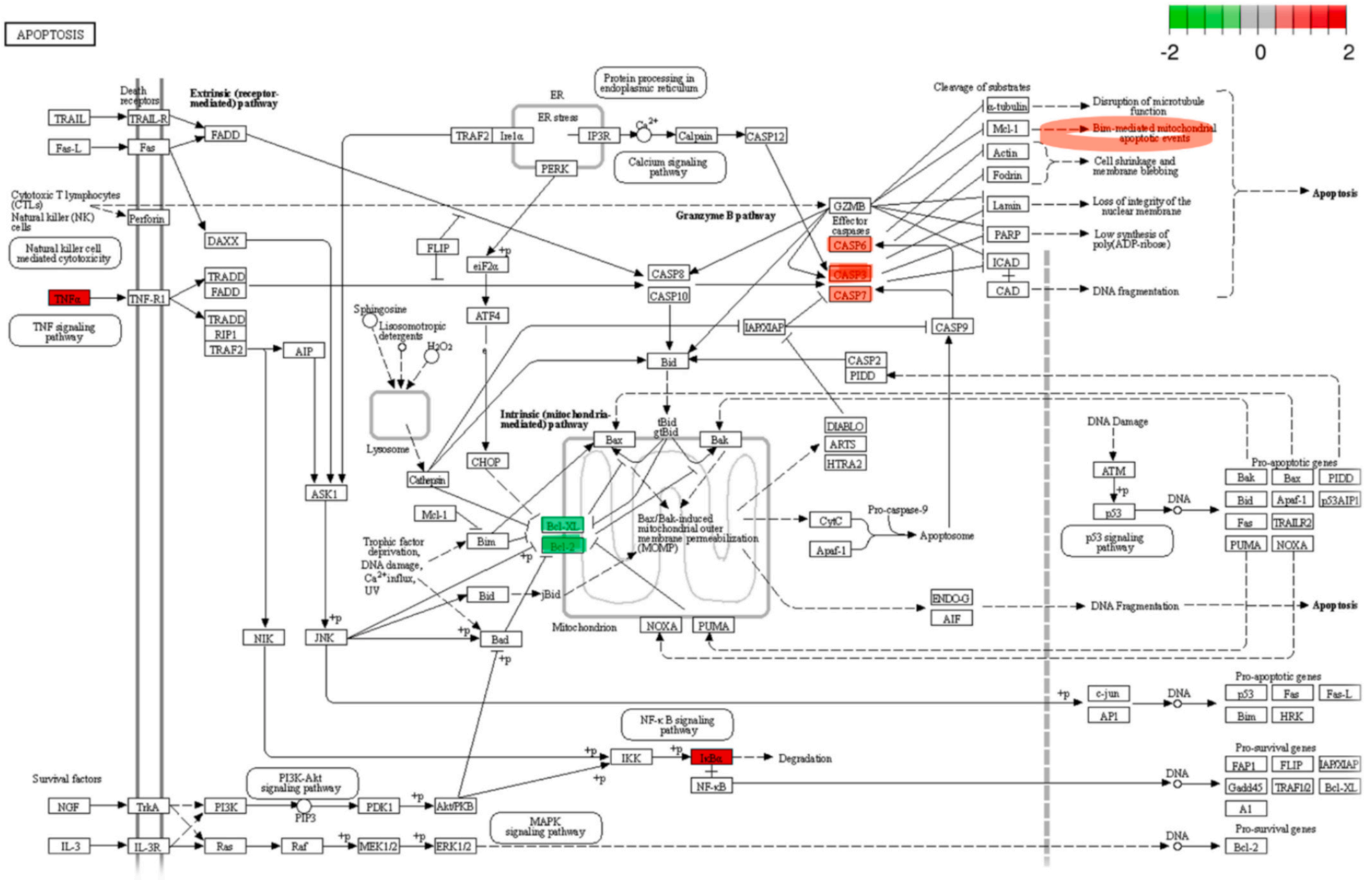

Fig. 6. Comprehensive apoptotic pathway map in HepG2 cells following AuNPs treatment. The diagram illustrates interconnected molecular mechanisms, including the death receptor (extrinsic) pathway via TRAIL/TNF receptors, the mitochondrial (intrinsic) pathway with Bcl-2 family regulation, and downstream caspase cascade activation. Red and green coloration (−2 to +2 scale) indicates upregulated and downregulated proteins, respectively, with caspases (particularly caspase-3/7) showing significant upregulation. The pathway culminates in characteristic apoptotic responses, including DNA fragmentation, membrane disruption, and cellular degradation. Arrows indicate activation sequences, while dashed lines represent indirect regulatory relationships between pathway components. (For interpretation of the references to colour in this figure legend, the reader is referred to the web version of this article.)

provides a mechanistic link between AuNPs exposure and the subsequently observed cytotoxicity in HepG2 cells, supporting intrinsic pathway activation as a primary mechanism of AuNPs-induced cell death.

3.6. Comprehensive apoptotic pathway mapping

Pathway analysis integrating all molecular and cellular observations revealed an intricate network of apoptotic signaling activated by AuNPs exposure in HepG2 cells (Fig. 6). The pathway map illustrated interconnected molecular mechanisms spanning both extrinsic and intrinsic apoptotic pathways. Extrinsic pathway activation was evidenced through death receptor (TRAIL/TNF) signaling components, with subsequent involvement of adaptor proteins such as FADD and initiator caspases. Intrinsic pathway engagement was demonstrated through mitochondrial components, particularly the BCL-2 protein family regulatory network. Heatmap-style colorimetric representation on the pathway map (−2 to +2 scale) revealed differential regulation patterns, with red coloration indicating upregulation and green indicating downregulation following AuNPstreatment. Notably, effector caspases (particularly caspase-3/7) showed significant upregulation despite the observed downregulation of CASP3 at the transcriptional level, suggesting post-transcriptional regulatory mechanisms or involvement of alternative caspases. The pathway culminated in characteristic apoptotic endpoints, including DNA fragmentation, membrane phosphatidylserine externalization, and cellular disintegration. Directional arrows within the pathway map indicated activation sequences, while dashed lines represented indirect regulatory relationships between pathway components, providing a comprehensive visualization of the molecular cascade leading to AuNPs-induced apoptosis in HepG2 cells.

3.7. Oxidative stress and antioxidant system perturbation

Extensive analysis of redox parameters revealed a significant downregulation of oxidative stress and an augmentation of the antioxidant defense system in HepG2 cells following AuNPs exposure (Table 2).

3.8. Enzymatic antioxidants

Among the enzymatic antioxidants, the most notable change was observed in SOD, which exhibited a significant increase of 30.0 % (from 5.27 ± 0.43 to 6.85 ± 0.62 U/mg protein, $p = 0.0018$), suggesting a compensatory response to the elevated oxidative stress. Similarly, CAT activity increased by 22.4 % (from 18.43 ± 1.72 to 22.56 ± 2.08 U/mg protein, $p = 0.0041$), indicating enhanced capacity to neutralize hydrogen peroxide. GPx activity was upregulated by 15.0 % (from 24.65 ± 2.31 to 28.36 ± 2.91 nmol/min/mg protein, $p = 0.0067$), further strengthening the antioxidant defense. GR and GST also exhibited significant increases of 18.3 % (from 15.87 ± 1.53 to 18.76 ± 1.67 nmol/min/mg protein, $p = 0.0129$) and 7.2 % (from 86.43 ± 7.92 to 92.67 ± 8.21 nmol/min/mg protein, $p = 0.0175$), respectively, contributing to

Table 2
Effect of Citrate-Capped AuNPs (50 μg/mL) on Antioxidant Defense and Oxidative Stress Markers in HepG2 Cells.

Parameters	HepG2 (No Treatment)	AuNPs (50 μg/mL)	% Change	P-value	Significance
SOD (U/mg protein)	5.27 ± 0.43	6.85 ± 0.62	+30.0 %	0.0018	**
CAT (U/mg protein)	18.43 ± 1.72	22.56 ± 2.08	+22.4 %	0.0041	**
GPx (nmol/min/mg protein)	24.65 ± 2.31	28.36 ± 2.91	+15.0 %	0.0067	**
GR (nmol/min/mg protein)	15.87 ± 1.53	18.76 ± 1.67	+18.3 %	0.0129	*
GST (nmol/min/mg protein)	86.43 ± 7.92	92.67 ± 8.21	+7.2 %	0.0175	*
GSH (nmol/mg protein)	28.76 ± 2.65	31.87 ± 3.09	+10.7 %	0.0023	**
Vitamin C (μg/mg protein)	3.42 ± 0.35	4.12 ± 0.42	+20.4 %	0.0082	**
Vitamin E (μg/mg protein)	1.87 ± 0.21	2.21 ± 0.24	+18.2 %	0.0097	**
MDA (nmol/mg protein)	0.89 ± 0.11	0.62 ± 0.08	−30.3 %	0.0004	***
Protein Carbonyl (nmol/mg protein)	1.56 ± 0.20	1.23 ± 0.18	−21.2 %	0.0009	***
ROS (% of control)	100.00 ± 9.32	61.75 ± 6.42	−38.3 %	0.0002	***

Values are presented as mean ± SD ($n = 6$ independent experiments). Statistical analysis performed using Student's t-test. Significance levels: * $p < 0.05$, ** $p < 0.01$, *** $p < 0.001$. **SOD**: Superoxide dismutase; **CAT**: Catalase; **GPx**: Glutathione peroxidase; **GR**: Glutathione reductase; **GST**: Glutathione S-transferase; **GSH**: Reduced glutathione; **MDA**: Malondialdehyde; **ROS**: Reactive oxygen species.

the maintenance of cellular redox homeostasis.

3.9. Non-enzymatic antioxidants

Regarding non-enzymatic antioxidants, GSH levels increased by 10.7 % (from 28.76 ± 2.65 to 31.87 ± 3.09 nmol/mg protein, $p = 0.0023$), reflecting a heightened capacity to neutralize free radicals. Additionally, vitamin C and vitamin E levels were significantly elevated by 20.4 % (from 3.42 ± 0.35 to 4.12 ± 0.42 μg/mg protein, $p = 0.0082$) and 18.2 % (from 1.87 ± 0.21 to 2.21 ± 0.24 μg/mg protein, $p = 0.0097$), respectively, further supporting cellular antioxidant defenses.

3.10. Oxidative stress markers

Regarding oxidative stress markers, the data revealed dramatic reductions in oxidative damage indicators following AuNPs treatment. MDA, a lipid peroxidation product, decreased by 30.3 % (from 0.89 ± 0.11 to 0.62 ± 0.08 nmol/mg protein, $p = 0.0004$), reducing lipid damage. Similarly, protein carbonyl content, an indicator of protein oxidation, was significantly reduced by 21.2 % (from 1.56 ± 0.20 to 1.23 ± 0.18 nmol/mg protein, $p = 0.0009$), suggesting decreased protein oxidation. ROS, a direct indicator of oxidative stress, was reduced by 38.3 % (from 100.00 ± 9.32 % to 61.75 ± 6.42 %, $p = 0.0002$), signaling a substantial decrease in ROS levels, which directly contributes to the protective effects against oxidative damage. These findings demonstrate that AuNPs treatment in HepG2 cells led to significant changes in antioxidant defense and oxidative stress parameters. Importantly, the upregulation of enzymatic and non-enzymatic antioxidants, alongside the reduction in oxidative stress markers, suggests a protective cellular response. The observed modulation of oxidative stress highlights the potential therapeutic role of AuNPs in mitigating oxidative damage and improving cellular redox balance. The data strongly support the idea that AuNPs-induced cytotoxicity in HepG2 cells involves a complex interaction with cellular redox homeostasis, resulting in enhanced antioxidant activity and reduced oxidative damage.

4. Discussion

The physicochemical properties of AuNPs critically influence their biological activities and potential therapeutic applications. Our synthesized citrate-capped AuNPs demonstrated several advantageous characteristics for biological applications. The mean diameter of 32.6 nm places these particles within what Bromma et al. [60] identified as the optimal size range (30–50 nm) for cellular internalization. Their research with various cell lines demonstrated that particles in this size range achieve maximal uptake through receptor-mediated endocytosis, particularly via clathrin-mediated pathways. The moderate size distribution (CV = 23.4 %) observed in our preparation is acceptable for biological applications, as Sonavane et al. [61] demonstrated that polydispersity indices below 0.3 (roughly equivalent to CV < 30 %) yield consistent biological responses.

The strong negative zeta potential (−35 ± 5 mV) conferred by the citrate capping layer provides excellent colloidal stability through electrostatic repulsion, preventing aggregation that could alter biological activity profiles. This stability parameter exceeds the conventional ±30 mV threshold considered necessary for long-term nanoparticle stability, as established by Bhattacharjee et al. [62]. Furthermore, the citrate capping specifically contributes to biocompatibility, as Freese et al. [63] demonstrated that citrate-stabilized AuNPs exhibit lower cytotoxicity toward normal cells compared to particles stabilized with synthetic polymers or cationic ligands. The crystallinity confirmed by XRD analysis represents another favorable characteristic, as Khlebtsov et al. [64] reported that highly crystalline gold nanostructures generate more defined SPR effects, potentially enhancing their interaction with biological systems through localized electromagnetic field effects. The SPR peak at 530 nm falls within the optimal range for biological applications, allowing potential theranostic applications combining optical imaging and photothermal therapy, as Chen et al. [65] demonstrated in their work with plasmonic nanoparticles of similar spectral characteristics.

The physicochemical properties characterized in our study, particularly the strong SPR and colloidal stability of AuNPs, align well with the design principles of emerging WaveFlex biosensors, which require mechanically stable and optically active nanoparticles for sensitive detection [66]. The potential adaptability of our AuNPs for such systems opens new avenues for integrating therapy with real-time monitoring, especially in the context of HCC, where early diagnosis is critical [67].

The differential cytotoxicity observed between normal WI-38 and cancerous HepG2 cells represents a promising finding with direct therapeutic implications. This selective toxicity aligns with observations by Nakhla et al. [68], who reported preferential toxicity of AuNPs toward MCF-7 breast cancer cells compared to normal cells. However, our study extends these findings to HCC, a particularly treatment-resistant cancer type with limited therapeutic options.

Several mechanisms likely contribute to this selective cytotoxicity. First, enhanced endocytosis rates in cancer cells may increase intracellular AuNPs accumulation. Behzadi et al. [69] demonstrated that cancer cells typically exhibit 2–5 fold higher nanoparticle uptake rates than normal counterparts due to their elevated metabolic activity and overexpressed surface receptors, particularly transferrin receptors that can facilitate AuNPs internalization. Additionally, Bhattacharya et al. [70] reported that cancer cells often display altered endosomal trafficking, potentially leading to differential intracellular distribution and processing of internalized AuNPs. Although differential cytotoxicity observed in vitro suggests a promising therapeutic window for citrate-capped AuNPs, quantitative assessment of this window and off-target toxicity remains to be determined. Future investigations incorporating in vivo models and broader toxicity assessments are essential to define the efficacy-safety balance and support translational development accurately [71].

Second, intrinsic metabolic differences between normal and cancer cells may contribute to selective vulnerability [72]. The Warburg effect, characterized by enhanced glycolysis and altered redox homeostasis in cancer cells, creates a baseline oxidative stress level that makes malignant cells more susceptible to additional ROS-generating insults [73–75]. Our observed 100 % increase in ROS levels may push already-stressed cancer cells beyond their adaptive capacity, while treated cells with robust antioxidant reserves can better withstand this oxidative challenge. This concept aligns with findings by [76,77], who described how oncogenic transformation typically compromises cellular antioxidant capacity while simultaneously increasing ROS production, creating an exploitable therapeutic window.

Third, altered apoptotic thresholds in cancer cells may enhance their sensitivity to AuNPs-induced cell death signals [78]. The complex pattern of apoptotic gene expression changes we observed, including simultaneous upregulation of both pro-survival (BCL-2) and pro-death (TP53) factors, may elicit different outcomes depending on the baseline apoptotic machinery configuration [79]. HepG2 cells, with their characteristically altered apoptotic regulators, may interpret these signals differently than normal cells with intact apoptotic regulation, as Hamida et al. [80] suggested in their comparative studies of AuNPs' effects on matched normal and transformed cell lines.

Our study's seemingly contradictory gene expression patterns—particularly the simultaneous upregulation of pro-survival BCL-2 and downregulation of pro-apoptotic BAX—present an intriguing mechanistic puzzle. Rather than indicating apoptosis resistance, these patterns likely reflect complex cellular stress responses that prove insufficient to prevent cell death. Galluzzi et al. [81] described similar "adaptive stress responses" where cells initially upregulate protective mechanisms when faced with cytotoxic insults, creating transient expression profiles that appear contradictory to the eventual cell fate. The upregulation of BCL-2 likely represents a compensatory mechanism attempting to preserve mitochondrial integrity through AuNPs treatment. This interpretation aligns with findings by Alshammari et al. [82], who reported that lipoic acid-AuNPs improve both pro-survival and pro-apoptotic signaling in cancer cells, with the balance ultimately favoring cell survival activation of protective pathways.

The significant upregulation of TP53 ($p = 0.0144$) represents a critical response to cellular stress, consistent with genotoxic or oxidative damage. While p53 typically promotes apoptosis by upregulating BAX and downregulating BCL-2, our observation of opposite effects suggests either TP53 dysfunction in HepG2 cells or activation of TP53-independent pathways. HepG2 cells express wild-type TP53, but its functionality may be compromised by altered post-translational modifications or disrupted downstream signaling, as Souza et al. [83] described in their review of context-dependent TP53 responses.

The upregulation of HO-1 further supports an adaptive stress response interpretation, as this enzyme represents a key component of cellular defense against oxidative damage. However, the ultimately observed cytotoxicity indicates that these protective responses were overwhelmed, possibly due to the sustained oxidative stress evidenced by dramatic increases in ROS, MDA, and protein carbonyl levels [84]. This pattern of initial adaptation aligns with the "hormesis model" described by Calabrese et al. [85] and Luna–López et al. [86], where moderate stressors induce protective responses that can be overwhelmed by persistent or severe challenges.

The pronounced mitochondrial membrane potential collapse observed in our Rh-123 assays represents a critical mechanistic finding that links upstream molecular events to eventual cell death outcomes. Mitochondrial depolarization is widely considered a "point-of-no-return" in cell death signaling, as it typically leads to cytochrome *c* release, apoptosome formation, and caspase activation, irrespective of the initial triggering stimulus [87,88]. The substantial MMP reduction we observed indicates severe bioenergetic compromise that would inevitably lead to cell death, even in the presence of upregulated survival factors like BCL-2 [89].

This mitochondrial dysfunction aligns with findings by [90], who reported that AuNPs of similar size induced mitochondrial damage in various cell types. However, our study provides a more detailed kinetic analysis with an established IC50 value of 28.48 μg/mL for mitochondrial effects. The close alignment between this mitochondrial IC50 and our cytotoxicity data suggests that mitochondrial damage directly determines cell death outcomes [91], consistent with the intrinsic pathway dominance in AuNP-induced apoptosis reported by [92].

Mechanistically, AuNPs may compromise mitochondrial function through several pathways. Direct physical interaction with mitochondrial membranes is possible, as Chen et al. [93] demonstrated that internalized AuNPs can localize to mitochondria and disrupt membrane integrity. Additionally, AuNP-generated ROS can directly oxidize cardiolipin, a mitochondria-specific phospholipid critical for maintaining membrane potential, as Iqbal et al. [94] revealed in their oxidative stress-induced mitochondrial dysfunction studies. The thiol reactivity of gold surfaces may also contribute, as Mahmoud et al. [95] reported that AuNPs can bind to and inactivate mitochondrial thiol proteins essential for respiration and membrane potential maintenance.

Although our results clearly demonstrate a significant reduction in intracellular ROS and MDA levels following AuNPs treatment, the precise molecular mechanisms underlying this redox reprogramming remain to be fully elucidated. Potential pathways may include Nrf2-mediated transcriptional activation of antioxidant enzymes, direct ROS scavenging via surface interactions, or stabilization of redox-sensitive proteins through thiol-gold interactions [96]. These hypotheses warrant further investigation. Additionally, while our study focused on AuNPs as a standalone treatment, future work comparing these effects to standard chemotherapeutic agents—many of which are known to induce oxidative stress as part of their cytotoxic mechanism—will be essential for positioning AuNPs within the broader therapeutic landscape and evaluating their unique advantage in redox modulation [97].

The significant improvements in antioxidant markers and reductions in oxidative stress parameters observed in our study suggest that citrate-capped AuNPs exert a protective, rather than cytotoxic, effect in HepG2 cells. Rather than inducing oxidative damage, the AuNPs appear to enhance the cellular redox balance. This is evident from the consistent upregulation of both enzymatic (SOD, CAT, GPx, GR, GST) and non-enzymatic (GSH, vitamin C, vitamin E) antioxidant defenses, all of which revealed statistically significant increases following treatment with 50 μg/mL AuNPs. For instance, SOD activity increased by 30.0 % ($p = 0.0018$), while GSH levels rose by 10.7 % ($p = 0.0023$), indicating an overall strengthening of the intracellular antioxidant network. Concurrently, oxidative stress markers such as MDA, protein carbonyls, and intracellular ROS levels were markedly reduced by 30.3 %, 21.2 %, and 38.3 %, respectively (all $p < 0.001$), indicating diminished lipid peroxidation, protein oxidation, and ROS burden. These changes collectively suggest that the AuNPs mitigate oxidative damage, possibly by directly interacting with cellular redox systems or modulating signaling pathways that regulate antioxidant gene expression [98]. Our use of well-characterized citrate-capped AuNPs and physiologically relevant exposure concentrations may account for the observed protective effects. The mechanisms underlying the antioxidant-promoting effects of AuNPs remain fully elucidated but may involve several plausible pathways. Unlike pro-oxidant metal nanoparticles that catalyze Fenton-like reactions, citrate-capped AuNPs may act as redox buffers or interact favorably with antioxidant enzymes [99]. Previous studies [100,101] have shown that AuNPs can bind to redox-active proteins, though these interactions may differ based on surface coatings. Moreover, low-dose AuNP exposure has been reported to activate the Nrf2 pathway, a master regulator of antioxidant defense, potentially explaining the coordinated upregulation of enzymatic antioxidants observed here.

While our findings demonstrate that AuNPs treatment significantly enhances antioxidant enzyme activities and reduces oxidative stress

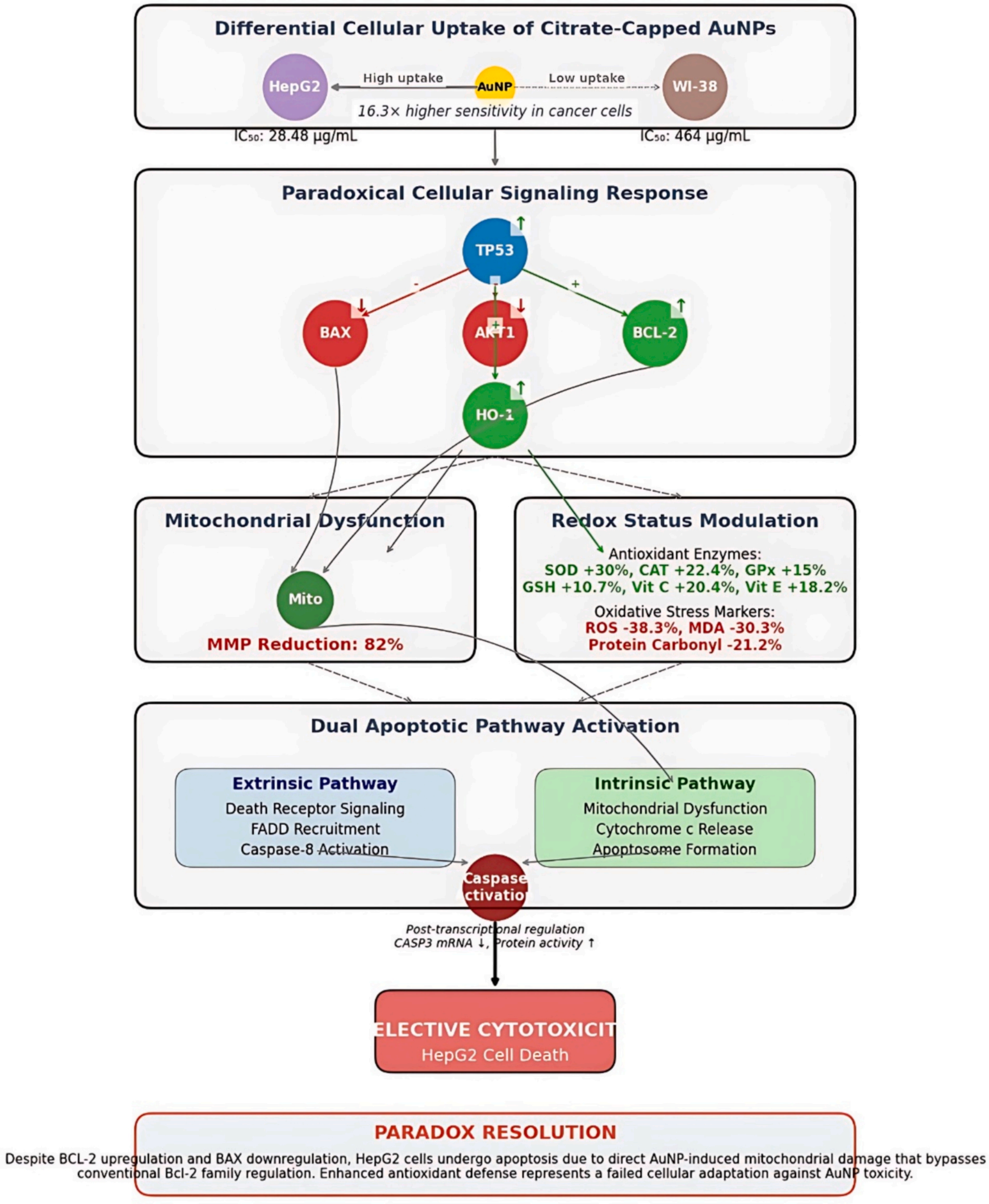

Fig. 7. Proposed mechanism of selective cytotoxicity induced by citrate-capped AuNPs in HepG2 cells. The schematic illustrates a multifaceted pathway where AuNPs preferentially accumulate in HepG2 cells, leading to paradoxical apoptotic signaling with TP53 upregulation, BCL-2 upregulation, and BAX downregulation. Despite this, mitochondrial membrane potential is severely disrupted, indicating BCL-2-independent mitochondrial damage. Enhanced antioxidant defenses (green) are accompanied by significant reductions in oxidative stress markers (red), suggesting a non-oxidative mechanism of cytotoxicity. Apoptosis proceeds through intrinsic and extrinsic pathways involving caspase activation and AKT1 downregulation. The "Paradox Resolution" highlights that protective cellular responses are insufficient to counterbalance the AuNPs-induced mitochondrial injury, leading to cancer-selective cell death. Green arrows denote upregulation; red arrows denote downregulation. Quantitative values are derived from experimental data. (For interpretation of the references to colour in this figure legend, the reader is referred to the web version of this article.)

markers within 24 h, the long-term consequences of this redox reprogramming remain unclear [102]. It is possible that prolonged or repeated exposure could lead to adaptive resistance, compensatory exhaustion, or altered redox signaling dynamics over time. Future studies will be required to assess the durability and biological significance of these antioxidant responses under chronic conditions, which will be crucial for evaluating the therapeutic viability and safety of AuNPs-based interventions [103].

The pathway analysis in our study illustrates how various cellular responses integrate into a complex network of molecular interactions leading to cell death. Activating extrinsic and intrinsic apoptotic pathways suggests multiple death-inducing stimuli converge to overcome potential resistance mechanisms. This dual pathway activation may explain the effectiveness of AuNPs against HepG2 cells, which are known for their resistance to conventional apoptotic stimuli through altered expression of death receptors and BCL-2 family proteins. Fulda and Vucic [104] highlighted this concept in their review of “apoptosis network convergence,” noting that simultaneous activation of multiple death pathways often overcomes resistance mechanisms that evolved against individual pathway activation—the selective toxicity toward cancer cells and the multi-pathway engagement present promising therapeutic implications. Conventional chemotherapeutics typically suffer from narrow therapeutic windows and significant toxicity toward normal tissues. Our observed differential cytotoxicity between HepG2 and WI-38 cells suggests that AuNPs might offer improved selective targeting. This selectivity could be further enhanced through surface functionalization with cancer-specific targeting ligands, as Samadian et al. [105] demonstrated, who conjugated folic acid to AuNPs to improve their specificity toward folate receptor-overexpressing cancer cells.

While the current analysis focused on apoptosis-related genes, future studies should expand to examine the expression of additional oncogenes and tumor suppressor genes across a range of AuNP concentrations. This would help delineate broader regulatory effects and identify potential off-target molecular consequences. Moreover, although the present study demonstrates the selective cytotoxic potential of citrate-capped AuNPs in vitro, comprehensive in vivo investigations of pharmacokinetics and bioavailability are necessary to understand better systemic distribution, organ accumulation, clearance mechanisms, and possible off-target effects—critical considerations for clinical translation. A key limitation of this study is the absence of combinatorial analyses with established chemotherapeutics or immunotherapies. Future work should explore whether citrate-capped AuNPs can potentiate the efficacy of agents such as 5-fluorouracil or oxaliplatin or modulate immune responses when combined with immunotherapies. Such studies may reveal synergistic interactions and offer new strategies to improve treatment outcomes in colorectal cancer and other malignancies. Another important limitation is the lack of investigation into potential immune responses triggered by AuNPs exposure. Although our in vitro model did not include immune cell types, it is well-documented that gold nanoparticles can influence immune signaling—either enhancing anti-tumor immunity or provoking inflammatory or hypersensitivity reactions. Thus, future in vivo studies using immunocompetent models are essential to characterize the immunomodulatory profile of citrate-capped AuNPs fully. Lastly, cytotoxicity assessments in this study were limited to a single cancer cell line (HepG2) and one normal cell line (WI-38). While these models provided valuable preliminary insights into selective cytotoxicity, responses may differ across cell types. Future studies should include a broader panel of cancerous and normal cells to establish the generalizability and specificity of AuNPs-induced cytotoxic effects, thereby strengthening the translational relevance of the findings.

Collectively, our findings reveal a complex yet coherent mechanism underlying the selective cytotoxicity of citrate-capped AuNPs in HepG2 cells (Fig. 7). The markedly lower IC50 in HepG2 cells compared to WI-38 normal fibroblasts underscores a differential uptake or sensitivity, favoring cancer-selective action. Interestingly, AuNPs treatment triggered paradoxical apoptotic signaling characterized by TP53 upregulation alongside unexpected BCL-2 upregulation and BAX downregulation—suggesting a cellular attempt at survival that ultimately fails. Despite this anti-apoptotic expression profile, we observed a profound loss of mitochondrial membrane potential (82 % reduction), indicating that mitochondrial dysfunction bypasses BCL-2 regulatory control. Additionally, AuNPs significantly enhanced the antioxidant defense system—elevating SOD, CAT, GPx, GSH, and HO-1—while simultaneously reducing oxidative stress markers such as ROS, MDA, and protein carbonyls. This suggests that oxidative stress is not the primary cytotoxic mechanism. Rather, the observed apoptosis proceeds via a non-canonical pathway involving direct mitochondrial injury, AKT1 downregulation, and post-transcriptional caspase activation. The overall mechanism reflects a dynamic interplay where compensatory antioxidant and survival responses are overwhelmed by AuNPs-induced mitochondrial disruption, selectively inducing death in HepG2 cells.

5. Conclusion

In conclusion, this study reveals that citrate-capped AuNPs selectively induce cytotoxicity in HepG2 cells through oxidative stress and mitochondrial dysfunction, sparing normal fibroblasts at therapeutic concentrations. The complex mechanistic pathways include a significant increase in ROS and oxidative damage, which overwhelm the cancer cells’ antioxidant defenses, leading to irreversible cellular damage and apoptosis. Pathway analysis shows activation of both intrinsic and extrinsic apoptotic mechanisms, which may help reduce the likelihood of resistance compared to single-target therapies. The differential sensitivity between cancer and normal cells suggests a promising therapeutic potential for AuNPs, leveraging cancer cells’ unique metabolic profiles and altered apoptotic thresholds. However, further in vivo validation, optimization of AuNPs properties, and exploration of synergistic treatments are necessary to realize the therapeutic potential of AuNPs fully. These findings contribute to the field of nanomedicine, offering a solid foundation for advancing AuNPs-based anti-cancer strategies for HCC treatment. While our in vitro findings demonstrate promising selective cytotoxicity and mechanistic insight into AuNPs-induced apoptosis, comprehensive in vivo studies addressing biodistribution, systemic toxicity, and clearance are warranted to fully evaluate the translational potential of these nanoparticles for therapeutic applications.

Declaration of competing interest

The authors declare that they have no known competing financial interests or personal relationships that could have appeared to influence the work reported in this paper.

Acknowledgments

Princess Nourah bint Abdulrahman University Researchers Supporting Project Number (PNURSP2025R446), Princess Nourah bint Abdulrahman University, Riyadh, Saudi Arabia.

Appendix A. Supplementary data

Supplementary data to this article can be found online at https://doi.org/10.1016/j.saa.2025.126630.

Data availability

All data generated or analyzed during this study are included in this published article (and its supplementary information files).

References

[1] T. El-Sewedy, A.F. Salama, A.E. Mohamed, N.M. Elbaioumy, A.H. El-Far, A. N. Albalawi, A. Elmetwalli, Hepatocellular carcinoma cells: activity of amygdalin and Sorafenib in targeting AMPK/mTOR and BCL-2 for anti-angiogenesis and apoptosis cell death, BMC Complement. Med. Ther. 23 (2023) 1–17.

[2] S.G. Abd Elnasser, A. Elmetwalli, A.A. Hamed, M.G. Bata, M.G. Hassan, Assessment of histological damage to rat liver induced by gold nanoparticles derived from Bacteria: preliminary investigation on dose-dependent effects, Benha, J. Appl. Sci. 9 (2024) 149–153.

[3] A. Elmetwalli, M.G. Hassan, A. Ahmed, M.O. Abdel-Monem, J. Hassan, Silver nanoparticles combined with chitosan demonstrate strong and targeted efficacy against pancreatitis, Benha, J. Appl. Sci. 9 (2024) 175–179.

[4] J.M. Llovet, R. Pinyol, R.K. Kelley, A. El-Khoueiry, H.L. Reeves, X.W. Wang, G. J. Gores, A. Villanueva, Molecular pathogenesis and systemic therapies for hepatocellular carcinoma, Nat. Can. 3 (2022) 386–401.

[5] B. Liu, H. Zhou, L. Tan, K.T.H. Siu, X.-Y. Guan, Exploring treatment options in cancer: tumor treatment strategies, Signal Transduct. Target. Ther. 9 (2024) 175.

[6] G. Bor, I.D. Mat Azmi, A. Yaghmur, Nanomedicines for cancer therapy: current status, challenges and future prospects, Ther. Deliv. 10 (2019) 113–132.

[7] M.G. Hassan, H.S. Farouk, D.M. Baraka, M. Khedr, M.E. El Awady, F. Ameen, Z. Sajjad, A. Elmetwalli, Pomegranate's silver bullet: nature-powered nanoparticles deliver a one-two punch against cancer and antimicrobial resistance, Inorg. Chem. Commun. 168 (2024) 112853.

[8] S. Alex, A. Tiwari, Functionalized gold nanoparticles: synthesis, properties and applications a review, J. Nanosci. Nanotechnol. 15 (2015) 1869–1894.

[9] A. Elmetwalli, T. El-Sewedy, M.G. Hassan, M.O. Abdel-Monem, J. Hassan, N. F. Ismail, A.F. Salama, J. Fu, N. Mousa, D.K. Sabir, Gold nanoparticles mediate suppression of angiogenesis and breast cancer growth via MMP-9/NF- B/mTOR and PD-L1/PD-1 signaling: integrative in vitro validation and network pharmacology insights, Naunyn, Schmiedebergs. Arch. Pharmacol. (2024) 1–19.

[10] A. Elmetwalli, M.O. Abdel-Monem, A.H. El-Far, G.S. Ghaith, N.A.N. Albalawi, J. Hassan, N.F. Ismail, T. El-Sewedy, M.M. Alnamshan, N.K. Alaqeel, Probiotic-derived silver nanoparticles target mTOR/MMP-9/BCL-2/dependent AMPK activation for hepatic cancer treatment, Med. Oncol. 41 (2024) 106.

[11] M.I. Anik, N. Mahmud, A. Al Masud, M. Hasan, Gold nanoparticles (GNPs) in biomedical and clinical applications: A review, Nano Sel. 3 (2022) 792–828.

[12] P. Pedrosa, R. Mendes, R. Cabral, L.M. Sa Martins, P.V. Baptista, A.R. Fernandes, Combination of chemotherapy and au-nanoparticle photothermy in the visible light to tackle doxorubicin resistance in cancer cells, Sci. Rep. 8 (2018) 11429.

[13] S.K. Vemuri, R.R. Banala, S. Mukherjee, P. Uppula, S. Gpv, G.R. Av, Novel biosynthesized gold nanoparticles as anti-cancer agents against breast cancer: synthesis, biological evaluation, molecular modelling studies, Mater. Sci. Eng. C 99 (2019) 417–429.

[14] U. Prabhakar, H. Maeda, R.K. Jain, E.M. Sevick-Muraca, W. Zamboni, O. C. Farokhzad, S.T. Barry, A. Gabizon, P. Grodzinski, D.C. Blakey, Challenges and key considerations of the enhanced permeability and retention effect for nanomedicine drug delivery in oncology, 2013.

[15] G. Wang, X. Jiang, P. Torabian, Z. Yang, Investigating autophagy and intricate cellular mechanisms in hepatocellular carcinoma: emphasis on cell death mechanism crosstalk, Cancer Lett. 216744 (2024).

[16] J. Wekalao, S.M. Njoroge, O. Elamri, Enhanced malaria detection using a hybrid borophene-based terahertz biosensor with random forest regression analysis, Brazilian, J. Phys. 55 (2025) 1–18.

[17] H. Zhou, D. Li, Q. Lv, C. Lee, Integrative Plasmonics: Optical Multi-Effects and Acousto-Electric-Thermal Fusion for Biosensing, Energy Conversion, and Photonic Circuits, Chem. Soc, Rev, 2025.

[18] R. Kuang, Z. Wang, L. Ma, H. Wang, Q. Chen, A.L. Junior, S. Kumar, X. Li, C. Marques, R. Min, Smart photonic wristband for pulse wave monitoring, Opto-Electronic Sci. 3 (2024) 240001–240009.

[19] W. Li, Y. Long, Y. Yan, K. Xiao, Z. Wang, D. Zheng, A. Leal-Junior, S. Kumar, B. Ortega, C. Marques, Wearable photonic smart wristband for cardiorespiratory function assessment and biometric identification, Opto-Electronic Adv. (2025) 240251–240254.

[20] S. Elmore, Apoptosis: a review of programmed cell death, Toxicol. Pathol. 35 (2007) 495–516.

[21] N. Bou Antoun, A.-M., Chioni, dysregulated signalling pathways driving anticancer drug resistance, Int. J. Mol. Sci. 24 (2023) 12222.

[22] Y. Min, G.G.D. Suminda, Y. Heo, M. Kim, M. Ghosh, Y.-O. Son, Metal-based nanoparticles and their relevant consequences on cytotoxicity cascade and induced oxidative stress, Antioxidants 12 (2023) 703.

[23] A. Glasauer, N.S. Chandel, Targeting antioxidants for cancer therapy, Biochem. Pharmacol. 92 (2014) 90–101.

[24] Z. He, Q. Xu, B. Newland, R. Foley, I. Lara-s ez, J.F. Curtin, W. Wang, Reactive oxygen species (ROS): utilizing injectable antioxidative hydrogels and ROS-producing therapies to manage the double-edged sword, J. Mater. Chem. B 9 (2021) 6326–6346.

[25] D. Mateo, P. Morales, A. Valos, A.I. Haza, Oxidative stress contributes to gold nanoparticle-induced cytotoxicity in human tumor cells, Toxicol. Mech. Methods 24 (2014) 161–172.

[26] J. Li, C. Chen, T. Xia, Understanding nanomaterial liver interactions to facilitate the development of safer nanoapplications, Adv. Mater. 34 (2022) 2106456.

[27] C.R. Gandhi, Oxidative stress and hepatic stellate cells: a paradoxical relationship, Trends Cell Mol. Biol. 7 (2012) 1.

[28] J. Xu, Y. Liu, Nanomaterials for liver cancer targeting: research progress and future prospects, Front. Immunol. 16 (2025) 1496498.

[29] A. Amanmadov, R. Durdyyev, M. Kotyrov, D. Melebaev, Synthesis of gold nanoparticles via citrate reduction and their characterization (2019) 34–42.

[30] M.K. Pitchan, S. Bhowmik, M. Balachandran, M. Abraham, Effect of surface functionalization on mechanical properties and decomposition kinetics of high performance polyetherimide/MWCNT nano composites, Compos. Part A Appl. Sci. Manuf. 90 (2016) 147–160.

[31] A.M. Alokda, A.A. Soffar, A.I. Yousef, F.A.R. Ibrahim, T. El-Sewedy, A. Elmetwalli, PFDN1 silencing disrupts critical cancer pathways in triple-negative breast cancer: investigating migration, cell cycle, and apoptosis as a new target therapy, Naunyn, Schmiedebergs. Arch. Pharmacol. (2025) 1–20.

[32] S. Lu, J. Liang, H. Long, H. Li, X. Zhou, Z. He, Y. Chen, H. Sun, Z. Fan, H. Zhang, Crystal phase control of gold nanomaterials by wet-chemical synthesis, Acc. Chem. Res. 53 (2020) 2106–2118.

[33] A. Kumar, N. Das, N.K. Satija, K. Mandrah, S.K. Roy, R.G. Rayavarapu, A novel approach towards synthesis and characterization of non-cytotoxic gold nanoparticles using taurine as capping agent, Nanomaterials 10 (2019) 45.

[34] M.G. Hassan, A.A. Hamed, A. Elmetwalli, M.O. Abdel-Monem, H.M. El-Shora, W. M. Alsallami, Assessment of myco-fabricated Al2O3 NPs toxicity on cancer cells and pathogenic microbes by suppression of bacterial metabolic key enzymes, Int. J. Biol. Macromol. 283 (2024) 137073.

[35] A.N. Al Balawi, J.G. Eldiasty, S.A.-E.R. Mosallam, A.R. El-Alosey, A. Elmetwalli, Assessing multi-target antiviral and antioxidant activities of natural compounds against SARS-CoV-2: an integrated in vitro and in silico study, Bioresour. Bioprocess. 11 (2024) 108.

[36] B.B. Nath, A.A. Babrekar, B. Parthasarathy, Assessment of cell viability in intact glandular tissue in Chironomus ramosus using dye-exclusion and colorimetric assays, Cytotechnology 49 (2005) 59–65.

[37] I.F. Gimenez, M.C. Anazetti, P.S. Melo, M. Haun, M.M.M. De Azevedo, N. Durn, O. L. Alves, Cytotoxicity on V79 and HL60 cell lines by Thiolated- -Cyclodextrin-au/Violacein nanoparticles, J. Biomed. Nanotechnol. 1 (2005) 352–358.

[38] A. Khatua, A. Prasad, E. Priyadarshini, A.K. Patel, A. Naik, M. Saravanan, H. Barabadi, Llora Ghosh, B. Paul, R. Paulraj, Emerging antineoplastic plant-based gold nanoparticle synthesis: a mechanistic exploration of their anticancer activity toward cervical cancer cells, J. Clust. Sci. 31 (2020) 1329–1340.

[39] A.A. El-Shehawy, A. Elmetwalli, A.H. El-Far, S.A.E.-R. Mosallam, A.F. Salama, A. O. Babalghith, M.A. Mahmoud, H. Mohany, M. Gaber, T. El-Sewedy, Thymoquinone, piperine, and sorafenib combinations attenuate liver and breast cancers progression: epigenetic and molecular docking approaches, BMC Complement. Med. Ther. 23 (2023) 1–21.

[40] A.N. Al Balawi, N.A.N. Alblwi, R. Soliman, A.H. El-Far, M.G. Hassan, T. El-Sewedy, F. Ameen, N.F. Ismail, A. Elmetwalli, Impact of vitamin D deficiency on immunological and metabolic responses in women with recurrent pregnancy loss: focus on VDBP/HLA-G1/CTLA-4/ENTPD1/adenosine-fetal-maternal conflict crosstalk, BMC Pregnancy Childbirth 24 (2024) 709.

[41] K.J. Livak, T.D. Schmittgen, Analysis of relative gene expression data using real-time quantitative PCR and the 2− ΔΔCT method, Methods 25 (2001) 402–408.

[42] M.P. Barde, P.J. Barde, What to use to express the variability of data: standard deviation or standard error of mean?, Perspect, Clin. Res. 3 (2012) 113–116.

[43] A. Baracca, G. Sgarbi, G. Solaini, G. Lenaz, Rhodamine 123 as a probe of mitochondrial membrane potential: evaluation of proton flux through F0 during ATP synthesis, Biochim. Biophys. Acta (BBA)-Bioenergetics. 1606 (2003) 137–146.

[44] R.A. Armstrong, When to use the B onferroni correction, Ophthalmic Physiol. Opt. 34 (2014) 502–508.

[45] P.T. Na Majtnerov, Rou ar, an overview of apoptosis assays detecting DNA fragmentation, Mol. Biol. Rep. 45 (2018) 1469–1478.

[46] I. Liesenborghs, J.S.A.G. Schouten, M. Kutmon, T.G.M.F. Gorgels, C.T. Evelo, W. H.G. Hubens, H.J.M. Beckers, C.A.B. Webers, L.M.T. Eijssen, A systematically derived overview of the non-ubiquitous pathways and genes that define the molecular and genetic signature of the healthy trabecular meshwork, Genomics 114 (2022) 110280.

[47] O.M. Ighodaro, O.A. Akinloye, First line defence antioxidants-superoxide dismutase (SOD), catalase (CAT) and glutathione peroxidase (GPX): their fundamental role in the entire antioxidant defence grid, Alexandria, J. Med. 54 (2018) 287–293.

[48] S. Marklund, G. Marklund, Involvement of the superoxide anion radical in the autoxidation of pyrogallol and a convenient assay for superoxide dismutase, Eur. J. Biochem. 47 (1974) 469–474.

[49] H. Aebi, [13] Catalase in vitro, in: Methods Enzymol, Elsevier, 1984, pp. 121–126.

[50] D.E. Paglia, W.N. Valentine, Studies on the quantitative and qualitative characterization of erythrocyte glutathione peroxidase, J. Lab. Clin. Med. 70 (1967) 158–169.

[51] I. Carlberg, B. Mannervik, [59] Glutathione Reductase, Methods Enzymol., Elsevier, in, 1985, pp. 484–490.

[52] W.H. Habig, W.B. Jakoby, [51] Assays for Differentiation of Glutathione S-Transferases, Methods Enzymol., Elsevier, in, 1981, pp. 398–405.

[53] M.A. Rahman, H. Hasegawa, M.A. Rahman, M.M. Rahman, M.A.M. Miah, Influence of cooking method on arsenic retention in cooked rice related to dietary exposure, Sci. Total Environ. 370 (2006) 51–60.

[54] S.T. Omaye, J.D. Turnbull, H.E. Sauberlich, [1] Selected Methods for the Determination of Ascorbic Acid in Animal Cells, Tissues, and Fluids, Methods Enzymol., Elsevier, in, 1979, pp. 3–11.

[55] I.D. Desai, [16] Vitamin E Analysis Methods for Animal Tissues, Methods Enzymol., Elsevier, in, 1984, pp. 138–147.

[56] H. Ohkawa, N. Ohishi, K. Yagi, Assay for lipid peroxides in animal tissues by thiobarbituric acid reaction, Anal. Biochem. 95 (1979) 351–358.

[57] R.L. Levine, D. Garland, C.N. Oliver, A. Amici, I. Climent, A.-G. Lenz, B.-W. Ahn, S. Shaltiel, E.R. Stadtman, [49] Determination of Carbonyl Content in Oxidatively Modified Proteins, Methods Enzymol., Elsevier, in, 1990, pp. 464–478.

[58] E. Eruslanov, S. Kusmartsev, Identification of ROS using oxidized DCFDA and flow-cytometry, Adv. Protoc. Oxidative Stress II. (2010) 57–72.

[59] H.-Y. Kim, Statistical notes for clinical researchers: effect size, Restor. Dent. Endod. 40 (2015) 328.

[60] K. Bromma, D.B. Chithrani, Advances in gold nanoparticle-based combined cancer therapy, Nanomaterials 10 (2020) 1671.

[61] G. Sonavane, K. Tomoda, K. Makino, Biodistribution of colloidal gold nanoparticles after intravenous administration: effect of particle size, Colloids Surf. B: Biointerfaces 66 (2008) 274–280.

[62] K. Bhattacharjee, B.L.V. Prasad, Surface functionalization of inorganic nanoparticles with ligands: a necessary step for their utility, Chem. Soc. Rev. 52 (2023) 2573–2595.

[63] C. Freese, C. Uboldi, M.I. Gibson, R.E. Unger, B.B. Weksler, I.A. Romero, P.-O. Couraud, C.J. Kirkpatrick, Uptake and cytotoxicity of citrate-coated gold nanospheres: comparative studies on human endothelial and epithelial cells, Part. Fibre Toxicol. 9 (2012) 1–11.

[64] N.G. Khlebtsov, L.A. Dykman, B.N. Khlebtsov, Synthesis and plasmonic tuning of gold and gold silver nanoparticles, Russ. Chem. Rev. 91 (2022).

[65] A.L. Chen, M.A. Jackson, A.Y. Lin, E.R. Figueroa, Y.S. Hu, E.R. Evans, V. Asthana, J.K. Young, R.A. Drezek, Changes in optical properties of plasmonic nanoparticles in cellular environments are modulated by nanoparticle PEGylation and serum conditions, Nanoscale Res. Lett. 11 (2016) 1–12.

[66] R.J. Albadr, W. Mohammedtaher, M. Alwan, M.J. Jawad, H. Mushtaq, M. Kedhim, A. Smerat, N. Msarhan, Experimental development of gold nanoparticle-based colorimetric sensor for simultaneous detection of triptan drugs in biological samples, Chem. Pap. 1–22 (2025).

[67] M. Bhange, D. Telange, Convergence of nanotechnology and artificial intelligence in the fight against liver cancer: a comprehensive review, Discov. Oncol. 16 (2025) 1–20.

[68] S. Nakhla, A. Rahawy, M. Abd El Salam, T. Shalaby, M. Zaghloul, E. El-Abd, Radiosensitizing and phototherapeutic effects of AuNPs are mediated by differential Noxa and Bim gene expression in MCF-7 breast cancer cell line, IEEE Trans. Nanobioscience 20 (2020) 20–27.

[69] S. Behzadi, V. Serpooshan, W. Tao, M.A. Hamaly, M.Y. Alkawareek, E.C. Dreaden, D. Brown, A.M. Alkilany, O.C. Farokhzad, M. Mahmoudi, Cellular uptake of nanoparticles: journey inside the cell, Chem. Soc. Rev. 46 (2017) 4218–4244.

[70] R. Bhattacharya, C.R. Patra, A. Earl, S. Wang, A. Katarya, L. Lu, J. N. Kizhakkedathu, M.J. Yaszemski, P.R. Greipp, D. Mukhopadhyay, Attaching folic acid on gold nanoparticles using noncovalent interaction via different polyethylene glycol backbones and targeting of cancer cells, nanomedicine nanotechnology, Biol. Med. 3 (2007) 224–238.

[71] A. Cammarata, J. Marino, M.N. Atia, H. Durn, R.J. Glisoni, Novel doxycycline gold nanoparticles via green synthesis using PEO-PPO block copolymers for enhanced radiosensitization of melanoma, Biomater. Sci. 5 (2025) 28–46.

[72] A. Schulze, A.L. Harris, How cancer metabolism is tuned for proliferation and vulnerable to disruption, Nature 491 (2012) 364–373.

[73] V. Bhardwaj, J. He, Reactive oxygen species, metabolic plasticity, and drug resistance in cancer, Int. J. Mol. Sci. 21 (2020) 3412.

[74] F. Ciccarone, M.R. Ciriolo, Modulation of cancer Cell Proliferation by Interfering with Metabolic ROS Production, in: Modul, Elsevier, Oxidative Stress, 2023, pp. 131–143.

[75] S. Arfin, N.K. Jha, S.K. Jha, K.K. Kesari, J. Ruokolainen, S. Roychoudhury, B. Rathi, D. Kumar, Oxidative stress in cancer cell metabolism, Antioxidants 10 (2021) 642.

[76] N.S. Aboelella, C. Brandle, T. Kim, Z.-C. Ding, G. Zhou, Oxidative stress in the tumor microenvironment and its relevance to cancer immunotherapy, Cancers (Basel) 13 (2021) 986.

[77] H.-Y. Liu, A.Z. Tuckett, M. Fennell, R. Garippa, J.L. Zakrzewski, Repurposing of the CDK inhibitor PHA-767491 as a NRF2 inhibitor drug candidate for cancer therapy via redox modulation, Investig. New Drugs 36 (2018) 590–600.

[78] V. Ramalingam, S. Revathidevi, T.S. Shanmuganayagam, L. Muthulakshmi, R. Rajaram, Gold nanoparticle induces mitochondria-mediated apoptosis and cell cycle arrest in nonsmall cell lung cancer cells, Gold Bull. 50 (2017) 177–189.

[79] N. Rahman, H. Khan, A. Zia, A. Khan, S. Fakhri, M. Aschner, K. Gul, L. Saso, Bcl-2 modulation in p53 signaling pathway by flavonoids: A potential strategy towards the treatment of cancer, Int. J. Mol. Sci. 22 (2021) 11315.

[80] R.S. Hamida, S.M. AlMotwaa, W.A. Al-Otaibi, H.A. Alqhtani, M.A. Ali, M.M. Bin-Meferij, Apoptotic induction by biosynthesized gold nanoparticles using Phormidesmis Communis strain AB_11_10 against osteosarcoma Cancer, Biomedicines 12 (2024) 1570.

[81] L. Galluzzi, I. Vitale, S.A. Aaronson, J.M. Abrams, D. Adam, P. Agostinis, E. S. Alnemri, L. Altucci, I. Amelio, D.W. Andrews, Molecular mechanisms of cell death: recommendations of the nomenclature committee on cell death, Cell Death Differ. 25 (2018).

[82] G.M. Alshammari, M.A. Abdelhalim, M.S. Al-Ayed, L.N. Al-Harbi, M.A. Yahya, The protective effect of -lipoic acid against gold nanoparticles (AuNPs)-mediated liver damage is associated with upregulating Nrf2 and suppressing NF- B, Nutrients 14 (2022) 3327.

[83] L.C.M. de e Souza, A. Faletti, C.P. Ver Ssimo, M.P. Stelling, H.L. Borges, p53 signaling on microenvironment and its contribution to tissue chemoresistance, Membranes (Basel). 12 (2022) 202.

[84] K.F. Zahra, R. Lefter, A. Ali, E.-C. Abdellah, C. Trus, A. Ciobica, D. Timofte, The involvement of the oxidative stress status in cancer pathology: a double view on the role of the antioxidants, Oxidative Med. Cell. Longev. 2021 (2021) 9965916.

[85] V. Calabrese, C. Cornelius, A.T. Dinkova-Kostova, E.J. Calabrese, M.P. Mattson, Cellular stress responses, the hormesis paradigm, and vitagenes: novel targets for therapeutic intervention in neurodegenerative disorders, Antioxid. Redox Signal. 13 (2010) 1763–1811.

[86] A. Luna Lopez, V.Y. Gonz Lez-Puertos, N.E.L. Pez-Diazguerrero, M.K. Nigsberg, New considerations on hormetic response against oxidative stress, J. Cell Commun. Signal. 8 (2014) 323–331.

[87] G. Kroemer, L. Galluzzi, C. Brenner, Mitochondrial membrane permeabilization in cell death, Physiol. Rev. 87 (2007) 99–163.

[88] H.L. Glover, A. Schreiner, G. Dewson, S.W.G. Tait, Mitochondria and cell death, Nat. Cell Biol. 26 (2024) 1434–1446.

[89] H.-D. Um, Bcl-2 family proteins as regulators of cancer cell invasion and metastasis: a review focusing on mitochondrial respiration and reactive oxygen species, Oncotarget 7 (2015) 5193.

[90] A. Gallud, K. Kl Ditz, J. Ytterberg, N. Stberg, S. Katayama, T. Skoog, V. Gogvadze, Y.-Z. Chen, D. Xue, S. Moya, Cationic gold nanoparticles elicit mitochondrial dysfunction: A multi-omics study, Sci. Rep. 9 (2019) 4366.

[91] C. Fernandes, A.J.C. Videira, C.D. Veloso, S. Benfeito, P. Soares, J.O.D. Martins, B. Goncalves, J.F.S. Duarte, A. Nio, M.S. Santos, P.J. Oliveira, Cytotoxicity and mitochondrial effects of phenolic and quinone-based mitochondria-targeted and untargeted antioxidants on human neuronal and hepatic cell lines: A comparative analysis, Biomolecules 11 (2021) 1605.

[92] H.R.H. Mohamed, B.A. Mohamed, G.M. Hakeem, S.H. Elnawasani, M. Nagy, R. Essam, A. Diab, G. Safwat, Cobalt oxide nanoparticles induce cytotoxicity and excessive ROS mediated mitochondrial dysfunction and p53-independent apoptosis in melanoma cells, Sci. Rep. 15 (2025) 2220.

[93] Y.-C. Chen, L.-C. Chang, Y.-L. Liu, M.-C. Chang, Y.-F. Liu, P.-Y. Chang, D. Manoharan, W.-J. Wang, J.-S. Chen, H.-C. Wang, Redox disruption using electroactive liposome coated gold nanoparticles for cancer therapy, Nat. Commun. 16 (2025) 3253.

[94] Y. Iqbal, F. Amin, M.H. Aziz, H.A. Alhadlaq, Z.M. Alaizeri, Biomimetic sodium alginate functionalized gold nanoparticles loaded with trans-resveratrol for in-vitro cancer treatment and intercellular ROS studies against MCF-7 cell lines, Colloids Surfaces A Physicochem. Eng. Asp. 712 (2025) 136448.

[95] E.-H.M. Mahmoud, L. Abdulsalam, E.-H. Moustafa, I.A. Alhanbali, S. Ullah, I. Ahmad, Anti-protozoan applications of the biogenic nanoparticles and their mechanism of action, Expand. Nanobiotechnology Appl. Commer., CRC Press (2025) 241–284.

[96] N. Jaiswal, N. Mahata, N. Chanda, Nanogold-Albumin Conjugates: Transformative Approaches for Next-Generation cancer Therapy and Diagnostics, Nanoscale, 2025.

[97] Y. Iqbal, S. Asghar, R. Hanif, W.J. Parak, F. Amin, PMA-coated gold nanoparticles functionalized with diamine-PEG conjugated with betulinic acid for in-vitro mitochondria-targeted anticancer and ROS detection study against MDA-MB-231 cell lines, Colloids Surfaces A Physicochem. Eng. Asp. 5 (2025) 137-170.

[98] H. Rizwan, J. Mohanta, S. Si, A. Pal, Gold nanoparticles reduce high glucose-induced oxidative-nitrosative stress regulated inflammation and apoptosis via tuberin-mTOR/NF- B pathways in macrophages, Int. J. Nanomedicine 5841–5862 (2017).

[99] M. Hepel, M. Stobiecka, Detection of oxidative stress biomarkers using functional gold nanoparticles, Fine Part. Med. Pharm. (2012) 241–281.

[100] J. Tournebize, A. Boudier, O. Joubert, H. Eidi, G. Bartosz, P. Maincent, P. Leroy, A. Sapin-Minet, Impact of gold nanoparticle coating on redox homeostasis, Int. J. Pharm. 438 (2012) 107–116.

[101] A. Goldstein, Y. Soroka, M. Fru i- Zlotkin, A. Lewis, R. Kohen, The bright side of plasmonic gold nanoparticles; activation of Nrf2, the cellular protective pathway, Nanoscale 8 (2016) 11748–11759.

[102] K.D. Patel, Z. Keskin-Erdogan, P. Sawadkar, N.S.A.N. Sharifulden, M.R. Shannon, M. Patel, L.B. Silva, R. Patel, D.Y.S. Chau, J.C. Knowles, Oxidative Stress Modulating Nanomaterials and their Biochemical Roles in Nanomedicine, Nanoscale Horizons, 2024.

[103] Z.A. Lockwood, M.R. Jirousek, J.P. Basilion, C. Burda, Redefining cancer Photodynamic Therapy with Gold Nanoparticles, Photochem, Photobiol, 2025.

[104] S. Fulda, D. Vucic, Targeting IAP proteins for therapeutic intervention in cancer, Nat. Rev. Drug Discov. 11 (2012) 109–124.

[105] H. Samadian, S. Hosseini-Nami, S.K. Kamrava, H. Ghaznavi, A. Shakeri-Zadeh, Folate-conjugated gold nanoparticle as a new nanoplatform for targeted cancer therapy, J. Cancer Res. Clin. Oncol. 142 (2016) 2217–2229.